Direct evidence for the interaction of stathmin along the length and the plus end of microtubules in cells

Roqiya Nouar, Gilles Breuzard, Sonia Bastonero, Svetlana Gorokhova, Pascale Barbier, François Devred, Hervé Kovacic, Vincent Peyrot

Direct evidence for the interaction of stathmin along the length and the plus-end of microtubules in cells

Roqiya Nouar[1 ¥], Gilles Breuzard[1 ¥ @], Sonia Bastonero[1], Svetlana Gorokhova[2], Pascale Barbier[1], François Devred[1], Hervé Kovacic[1] and Vincent Peyrot[1 @]

[1] Aix-Marseille Université, INSERM UMR_S 911 CRO2, Faculté de Pharmacie, 27 bd Jean-Moulin, 13385, Marseille, France

[2] Aix-Marseille Université, INSERM UMR_S 910 GMGF, Faculté de Médecine, 27 bd Jean-Moulin, 13385, Marseille, France

[¥] These authors contributed equally to this work.

[@] Corresponding authors: vincent.peyrot@univ-amu.fr; gilles.breuzard@univ-amu.fr

Running title: Stathmin binds to microtubules in cells

ABBREVIATIONS

FITC: fluorescein isothiocyanate; FRET: Förster Resonance Energy Transfer; Immuno-FRET: immunofluorescence resonance energy transfer; MT: microtubule; NFRET: normalized fluorescence resonance energy transfer; FRAP: Fluorescence Recovery After Photobleaching; ROI: region of interest; pSer25-, pSer38-, pSer16-, pSer63-stathmin: stathmin phosphorylated on serine 25, 38, 16, 63, respectively; TRITC: tetramethylrodhamin isothiocyanate;

ABSTRACT

Stathmin is a prominent destabilizer of microtubules (MTs). Extensive *in vitro* studies suggest strongly that stathmin could act by sequestering tubulin and/or by binding to the MT tips. In cells, the molecular mechanisms of stathmin binding to tubulin and/or MTs and its implications for the MT dynamics remain unexplored. Using immunofluorescence resonance energy transfer and fluorescence recovery after photobleaching, we analysed the ability of stathmin and its phospho-forms (on Ser16, 25, 38 and 63) to interact with tubulin and MTs in A549 cells. Consistent with *in vitro* studies, we detected stathmin-tubulin interactions at the MT plus-ends and in the cytosol. Interestingly, we also observed a novel pool of stathmin bound along the MT. The expression of truncated stathmin and the use of MT-stabilizing taxol further showed that the C-terminal domain of stathmin is the main contributor to this binding, and that the phosphorylation state of stathmin plays a role in its binding along the MT wall. Our findings demonstrate that stathmin binds directly along the MT wall. This pool of stathmin would be readily available to participate in protofilament dissociation when the moving plus-end of a depolymerizing MT reaches the stathmin molecules.

KEYWORDS: stathmin/oncoprotein 18, tubulin, binding, immuno-FRET, FRAP.

INTRODUCTION

In eukaryotic cells, stathmin or oncoprotein 18 is one of the most prominent destabilizers of microtubule (MT) dynamics (1–3). Recent studies support a role for stathmin in the regulation of cell growth and motility, and show its involvement in human malignancies (4). The MT-destabilizing action of stathmin remains unclear: the best accepted mechanism is one whereby stathmin reduces MT polymer by sequestering two soluble α/β-tubulin dimers to form a curved complex (T2S) (2,5). This ternary complex is stable and unable to assemble into MT. Another model holds that stathmin may induce MT shrinkage (called 'catastrophe') directly by acting on its tips. Gupta et al. have recently shown that stathmin binds tightly to dolastatin-10 tubulin rings, which mimic curved tubulin protofilaments at MT plus-ends, and that stathmin depolymerizes stabilized protofilament-rich polymers (6). Using computer simulation, they found strong evidence for the promotion of catastrophe by stathmin through binding to the tips of MTs.

Several *in vitro* studies have sought to identify the stathmin domains that participate in tubulin binding (6–8). Using structural and biochemical approaches, Steinmetz et al. demonstrated with different truncated forms of stathmin that (i) under MT polymerizing conditions, the α-helical domain of stathmin was sufficient to stabilize tubulin heterodimers, (ii) the 40 N-terminal amino acid residues of stathmin were necessary to prevent further longitudinal stathmin-tubulin complex aggregation, and (iii) a precise length of the C-terminal domain of stathmin was necessary to form a stable ternary complex with tubulin heterodimer (9).

Stathmin activity is mainly regulated by phosphorylation on four serines (Ser16, Ser25, Ser38 and Ser63) (10–12). It has been shown in cells that Ser25 and Ser38 are phosphorylated first, followed by phosphorylation on Ser16 and Ser63 to produce a completely inactive tetra-phosphorylated form (11,13,14). The impact of individual phosphorylation has been thoroughly studied *in vitro* using purified stathmin modified by directed mutagenesis. Stathmin phosphorylated at either Ser16 or Ser63 shows a drastic loss of affinity for tubulin dimers, whereas di-phosphorylated stathmin (on Ser25 and Ser38) still binds to tubulin, though with a reduced affinity (15,16). Immunofluorescence studies of stathmin and MTs in solution have shown that both unphosphorylated and double Ser25/Ser38-phosphorylated stathmin can bind along the entire MT as well as on free tubulin (16,17). Despite these extensive *in vitro* studies, the molecular mechanisms of stathmin binding to tubulin and/or MTs, and the effect of phosphorylation on this process, remain poorly understood, especially in the cell microenvironment.

Förster resonance energy transfer (FRET) can be used to detect the proximity between two fluorophores separated by distances of 1–10 nm (18). Classically measured by fluorescence spectroscopy, FRET can also be measured by fluorescence microscopy. Since FRET occurs over distances similar to the size of proteins, it can be used to extend the resolution of the fluorescence microscope (typically > 250 nm) to detect protein-protein interactions. FRET microscopy is thus a powerful technique to determine whether proteins that are co-localized

at light resolution microscopy interact with one another in cells. In this way, Niethammer et al. developed an interesting FRET-based sensor with the expression of a double fluorescent stathmin fused to CFP on its N-terminal end and YFP on its C-terminus in Xenopus A6 cells (19). The FRET signal is scattered for free stathmin, owing to its high flexibility, but decreases when stathmin interacts with tubulin. In their model, they observed an anterograde gradient of the FRET signal from the perinucleus to the lamellipodia of cells, presumed to reflect differential phosphorylation of stathmin. However, direct labeling of proteins by fusing to fluorescent tags alters the protein itself and/or its endogenous level in the cell.

By examining several methodological aspects, numerous recent studies demonstrate that indirect double-labeling immunofluorescence of proteins combined with fluorescence microscopy is a valid method to identify association of proteins by FRET in cells (20–23). In our study, we mapped and characterized the stathmin–tubulin/MT interactions directly in cells using immunofluorescence resonance energy transfer (immuno-FRET) and fluorescence recovery after photobleaching (FRAP) microscopy. Consistent with the *in vitro* studies, we detected stathmin-tubulin interactions in the cytosol and at the plus-ends of the MTs. Interestingly, we observed stathmin puncta along the MT length. We also found that this interaction occurred mostly through the C-terminal domain of stathmin. Focusing on the phosphorylation state of stathmin, we observed that Ser25- and/or Ser38-phosphorylated stathmin were bound to the MT wall. Based on our results, we propose a novel dynamic model for the role played by stathmin in MT disassembly.

MATERIALS AND METHODS

Cell culture, cDNA cloning

The human non-small lung carcinoma cell line (ATCC, clone A549; CCL2, MD, USA) was routinely grown at 37 °C in a humidified atmosphere of 5% CO_2, and maintained by regular passage in a complete medium composed of RPMI 1640 (Lonza, France) supplemented with 10% heat-inactivated fetal bovine serum (Invitrogen, France). Cells were free of mycoplasma as evidenced by mycoalert tests (Lonza). For treatment with taxol (M_r = 853.91 g/mol, in DMSO; Seripharm, France), cells were incubated with 1–50 nM taxol for 4 h at 37 °C before observations. For plasmids, full stathmin was initially subcloned into pEGFP-C1 vector (high expression pCMV promotor, ClonTech, CA, USA) between the XhoI site (forward primer: 5'-CCGCTCGAGCGGGTGGCTTCTTCTGATATCCAGG-3') and the PstI site (reverse primer: 5'-GCTGACGAGACTGAAGCTGACTAAGCTGCAGC-3'). Two mutants of stathmin were constructed: the 'ΔCter-stathmin' insert encoding for stathmin deleted from Lys100 to Glu147 and mutated on Ser16, Ser25, Ser38 and Ser63 to Ala (7); and the 'ΔNter-stathmin' insert encoding for stathmin deleted from Met1 to Ser40 plus from Glu141 to Asp149 and mutated on Ser63 to Ala (9). The two genes were subcloned into a pEGFP-C1 vector as for the full stathmin, between the BglII (forward primer, respectively: 5'-TTAGATCTCCACCATGGCTTCTTCTGATATCC-3' and 5'-TTAGATCTCCACCATGAAGAAGAAGGATCTTTCCCTG-3') and BamHI site (reverse primer, respectively: 5'-TTTGGATCCCTAGTCGGCCTCTTCTGCCATTTTACTG-3' and 5'-TTTGGATCCTTATTATTTGGATTCTTTGTTCTTCCGC-3'). The pEGFP-tubulin plasmid was purchased from Invitrogen (Cergy-Pontoise, France). The pmCherry-tubulin plasmid encoding for wild-type α1B isotype was a gift from Dr Saudou (24).

Antibodies and immuno-blotting

We used, according to supplier's instructions, mouse monoclonal anti-α-tubulin antibody (Sigma-Aldrich, 1 mg/mL, clone DM1A recognizing epitope between amino acids 426 to 430), mouse monoclonal anti-vinculin antibody (Sigma-Aldrich, 1 mg/ml, clone hVIN-1), rabbit polyclonal anti-stathmin antibody (Sigma-Aldrich, 1 mg/mL) targeting the sequence of stathmin between amino acids 132 and 149, and recognizing all phosphorylated and unphosphorylated forms of stathmin, and rabbit monoclonal anti-pSer63 stathmin (Abcam, 1 mg/mL). Antisera containing rabbit polyclonal anti-pSer16, anti-pSer25 and anti-pSer38 antibodies were kindly given by Prof. Sobel (Institut du Fer à Moulin, UPMC, Paris, France) (25).

Phosphorylation of stathmin was analyzed by Western blotting in denaturing conditions (Fig. S3A): cells were lyzed by re-suspension in RIPA buffer (150 mM NaCl, 0.1% Triton X-100, 0.5% sodium deoxycholate,

0.1% SDS, 50 mM Tris-HCl pH 8.0), and lysates were centrifuged at 14,000 rpm for 20 min at 4 °C; equivalent quantities of proteins from the supernatant fraction underwent 15% denaturing in SDS-PAGE; proteins were blotted with anti-stathmin antibody (dilution 1:2000), anti-pSer25/pSer38/pSer16-stathmin antibodies (dilution 1:800 each) or anti-pSer63 antibody (dilution 1:1000). The anti-vinculin antibody (dilution 1:1000) was the reference. For analysis of phospho-stathmin by non-denaturing Western blotting (Fig. S2B), cells were lyzed by re-suspension in extraction buffer (50 mM Hepes pH 7.6, 150 mM NaCl, 5 mM EDTA, 10% glycerol, 0.1% Triton X-100, 10 mM 2-mercaptoethanol) and lysates were centrifuged at 12,000 rpm for 10 min at 4 °C. Equivalent quantities of proteins from the supernatant fraction underwent 15% non-denaturing PAGE. All blots were visualized using chemiluminescent HRP substrate Immobilon Western kit (Millipore) with G:Box driven by GeneSys software (Syngene, UK), and quantified by densitometry with ImageJ.

Immunofluorescence and transfection of cells

Cells were fixed with 4% paraformaldehyde in PBS pH 7.4 for 20 min at room temperature, and permeabilized with Triton X-100 0.5% (Sigma-Aldrich, France) in PBS for 10 min at room temperature. Immunostaining was carried out overnight with primary anti-α-tubulin (dilution 1:1000) and anti-total-stathmin antibodies (dilution 1:2000), anti-pSer16, pSer25, anti-pSr38 antibodies (dilution 1:1000 each). Next, cells were incubated for 1 h at room temperature in darkness with secondary FITC- and TRITC-conjugated antibodies (dilution 1:200 each from 1.5 mg/mL; Jackson Immunoresearch, USA). For direct immunofluorescence, primary anti-total-stathmin antibody was chemically coupled to the Atto532 fluorophore using a Lightening-Link™ Atto532 kit as recommended by Innova Bioscience, UK. Coverslips were mounted with a drop of ProLong® anti-fade solution (Invitrogen). For FRET and FRAP performed on living cells, the transient overexpression of the full stathmin, the ΔCter-stathmin and the ΔNter-stathmin coupled to EGFP protein was performed using the lipofection of cells with lipofectamine 2000 according to the Invitrogen protocol. Cells were also transfected to overexpress mCherry-tubulin (as acceptor). Here, 0.4 µg plasmid (0.2 µg + 0.2 µg coding for the donor and acceptor, respectively) was used.

Instrumentation and image acquisition

Imaging was performed on a Leica SP5 confocal laser scanning microscope (CLSM) with a Leica inverted microscope, equipped with a Plan-Apochromat 63× oil immersion objective (NA = 1.4). For all FRET experiments (immuno-FRET on fixed cells and FRET on living cells), images were recorded with the CLSM spectral mode selecting specific domains of the emission spectrum (26). The FRAP experiments were divided into three sequences as described elsewhere (26). The photobleaching of stathmin was carried out on a 2 µm

radius circular area of the lamellipodium regions containing MTs. This step used the 488 nm wavelength laser with 10 iterations of 2 µs/pixel. To determine MT dynamics, materials, acquisition of time-lapse series and analysis of the MT dynamic instability are described elsewhere (26).

The surface area of the microtubule network in the 200 µm² regions of interest (ROI) was measured by systematically executing Otsu's method *via* the plugin 'Otsu threshold' of ImageJ. This algorithm is an implementation of the Otsu thresholding technique (27). The histogram of pixel intensities is divided into two classes and the inter-class variance is minimized. This plugin outputs a binary image of MT and the ratios of MT on ROI surfaces are then calculated as percentages. With untreated cells, we found that 31 ± 4 % of the cell interior was occupied by the fluorescent microtubule network. As expected there was no impact of 1 nM taxol on the ratio of MT to ROI surface areas in treated cells. All these values come close to the range of 34-41% of tubulin in microtubules in tissue cultured cells previously determined by Ostlund et al. (28).

FRET calculation

FRET images were corrected from both background (collected outside cells on images) and cross-talk between donor and acceptor channels using Youvan's method (29):

(1) $Fc = I_{FRET} - A \times I_D - B \times I_A$

where I_{FRET}, I_D, and I_A were intensities (after background subtraction) in ROI of the FRET, donor (FITC or EGFP) and acceptor (TRITC, Atto532 or mCherry) channels, respectively. Parameters A and B were respectively the fraction of donor and acceptor leak-through into the FRET channel, and were calculated by quantifying the intensity ratios between images from cells labeled or expressing only the donor or the acceptor. In our study, the values of A and B were 0.15 and 0.02 on average, respectively. No leak-through signal from the donor into the acceptor channel or *vice versa* was observed.

Fc was therefore normalized to the direct acceptor signal using Wouters' method (30):

(2) $NFRET = Fc / I_A$

Calculations were performed from the variation in pixel response with the PixFRET plug-in of ImageJ in ROI (31). All positive pixels positive were pixels with NFRET intensity greater than 0. The NFRET intensities of 8-bit images were initially spread from 0 to 12 and from 0 to 30 on the 256-grayscale for respectively the FITC-TRITC/Atto532 pairs and the EGFP-mCherry couple, the maximum of which corresponds to 5% and 12% of NFRET in cells (32). FRET images were filtered with a 1-pixel-range median filter to reduce background noise. For FRET quantifications, images showing the NFRET distributions were merged with the tubulin/MT-labeling images, and ROIs of 200 µm² were outlined in the cell periplasm. NFRET hotspots co-localizing with MTs and outside MTs ('in the cytosol') were then counted and expressed per unit surface area (µm²) of MT and cytosol (e.g with untreated cells, ROIs of 200 µm² were divided into ~62 µm² and ~138 µm² for MT and cytosol,

respectively). We considered a 'NFRET hotspot' every pixel or cluster of pixels with NFRET intensities > 0% and surrounded by pixels of with nil intensity.

Fitting of FRAP data

Fluorescence recovery was extracted from images recorded in the bleached area and corrected for experimental fluctuations during acquisition. In all, 7–15 separate FRAP measurements were made in three independent experiments, and data were independently single-normalized as (33):

(1) $F_{\text{frap-norm}}(t) = [F_{\text{frap}}(t) - F_{\text{bg}}(t)] / F_{\text{frap-pre}}$

where $F_{\text{frap}}(t)$ corresponds to the fluorescence recovery in the bleached ROI at time t; $F_{\text{bg}}(t)$, the fluorescence intensity in a background ROI outside the cells, and $F_{\text{frap-pre}}$, the mean fluorescence intensity of bleached ROIs before the bleach after background subtraction:

(2) $F_{\text{frap-pre}} = \{\sum_{(t=0;\ t\ \text{bleach-1})} \{[F_{\text{frap}}(t) - F_{\text{bg}}(t)] / f_{\text{prebleach}}\}$

with $f_{\text{prebleach}}$ corresponding to five frames during the pre-bleaching period. In FRAP, the rate of fluorescence recovery reflects diffusion and binding dynamics. The next step in FRAP analysis is to ascertain the respective contributions of diffusion and binding to the fluorescence recovery curves.

First of all, we examined whether diffusion could be ignored or not (see Fig. S3). The results indicate that diffusion is so fast relative to binding that it can be ignored. Hence, the fluorescence recovery curve reflects the binding interactions. Later, recovery curves were fitted using a binding-dominant model given by (34,35):

(3) $F(t) = F_{\infty} - C_{\text{eq}}.\exp^{-k_{\text{off}}.t}$

The kinetic curves were analyzed for single exponential by nonlinear least-squares fitting based on the Levenberg-Marquardt algorithm to adjust F_{∞}, the fluorescence intensity at infinite time, C_{eq}, the fraction of fluorescence at equilibrium due to binding, and the dissociation rate constant k_{off}. This model was applied with no foreknowledge of either the geometry of the bleaching or the process of fluorescence recovery.

Using k_{off} from the curve fit, the pseudo first-order binding constant, k^*_{on}, was calculated by:

(4) $k^*_{\text{on}} = C_{\text{eq}}.k_{\text{off}} / (1 - C_{\text{eq}})$

And the turnover time was calculated by:

(5) $t_{1/2} = \ln 2 / k_{\text{off}}$

Statistical analysis

Data are presented as mean ± s.e.m, except for the FRET experiments performed with stathmin mutants presenting mean ± SD. The NFRET hotspots count, the percentage of MT plus-ends with NFRET hotspots and the quantification of stathmin phosphoforms by Western-blot were analyzed by Student's t test. Reported p-

values are two-sided and $p < 0.01$ was considered statistically significant. Asterisks in graphs indicate significant level *vs* control (*) $p < 0.01$, (**) $p < 0.001$. Statistical analyses were performed using Microsoft Excel software.

RESULTS

Immuno-FRET reveals that stathmin interacts with microtubules and cytosolic tubulin.

The spatial distribution of the interaction between tubulin and MT with endogenous stathmin was determined in A549 cells fixed with paraformaldehyde. Here, we performed immuno-FRET of α-tubulin using a secondary antibody coupled to FITC as FRET donor. Stathmin was detected using a primary antibody specific to unphosphorylated and phosphorylated stathmin ('total-stathmin' on figures), and then with a secondary antibody coupled to TRITC as FRET acceptor (Fig. 1A). The immunolocalization of stathmin yielded punctuated staining in the cytoplasm as previously described (25), which sometimes co-localized with the MTs (white arrows in region of interest ROI 1, lower panel) and with weakly labeled tubulin in the cytosol (arrows in ROI2). On the right panels, the normalized fluorescence resonance energy transfer (NFRET) signal was observed in pixel clusters, which we name NFRET hotspots. Beneath NFRET image, we superimposed images of the α-tubulin staining (gray in figure) with NFRET signal (purple) and we observed that these NFRET hotspots are located in the cytosol (arrows in ROI2), probably representing stathmin-tubulin complexes, and at the ends of MTs (blue arrowhead in ROI1). Interestingly, we observed NFRET hotspots throughout the length of MTs (arrows in ROI1).

NFRET images were obtained using Wouters normalization, for which possible artifacts can occur, as previously well described (36). To validate the significance of the measured NFRET signals in spots we compared the quenched and unquenched FITC donor emission after specific TRITC acceptor photobleaching (Fig. 1B, panels in false colors). Prior to TRITC photobleaching ('pre-bleaching – recovery' images), fluorescence emission of MTs was partially quenched when there were co-localized spots of stathmin (arrows). After the TRITC photobleaching ('post-bleaching – recovery' images), a recovery of the fluorescence of MT was observed where spots of stathmin occurred before the acceptor bleaching. At these bleached areas (n = 5 cells), we calculated a significant NFRET efficiency (37), on average $\%E = 4.5 \pm 1.3$. No relevant fluorescence intensity fluctuation in the channels of donor ($\%E = 1.1 \pm 0.9$) and acceptor ($\%E = 0.5 \pm 0.9$) was measured inside the 'control' region. Our observations confirm the interactions between stathmin and tubulin/MT as NFRET hotspots in cells.

Two experimental controls were performed to validate the range of NFRET efficiencies (Fig. S1A-B). As a negative control for NFRET (Fig. S1A), cells expressing the free EGFP (as donor) were fixed, followed by indirect immunofluorescent labeling of α-tubulin (secondary antibody coupled to TRITC, as acceptor). As expected, we observed no FRET signal, despite the apparent co-localization of EGFP and tubulin. As a positive control for NFRET (Fig. S1B), we performed an indirect immunofluorescent labeling of α-tubulin using two secondary antibodies, one coupled to FITC and the other to TRITC. On the images, MTs are yellow because of the superimposition of co-labeled tubulin. The NFRET signal is continuous over the entire length of MTs, with

an efficiency value between 1% and 5%. This double labeling of tubulin is ideal for obtaining the highest NFRET efficiency: a closely similar NFRET efficiency is observed for the interaction of stathmin with tubulin/MTs. Lastly, in order to rule out the possibility of artifacts due to large size or misorientation of secondary antibody complexes, we used direct immunofluorescence of α-tubulin (antibody coupled to FITC, as donor) and total-stathmin (coupled to Atto532, as acceptor) (Fig. S1C). The NFRET signals were still observed in hotspots within the same range of NFRET efficiency, indicating that the two immunofluorescence approaches were equivalent in our cell model. All these experiments confirm that immuno-FRET is well-suited to explore the interaction of stathmin with tubulin and/or MTs in cells.

Using FRET, we clearly demonstrate in cells that stathmin interacts with tubulin in the cytosol, as well as throughout the lengths and at the plus-ends of MTs. The interaction at the plus-ends of MTs is consistent with prior *in vitro* observations (6). Our data are consistent with a model where stathmin acts at MT ends. More surprising is the interaction of stathmin with the MT wall. Gupta and co-workers suggest that stathmin does not bind significantly to the MT lattice. By contrast, phosphoforms of stathmin, i.e. double phosphorylation of stathmin on Ser25 and Ser38, bind to MTs (16,17). We therefore went on to explore, by immuno-FRET, the binding of phosphorylated forms of stathmin with tubulin and/or MTs and their localization.

Stathmin phosphorylated on serine 38 and/or 25 interacts with microtubules.

The destabilizing activity of stathmin is attenuated by phosphorylation of four serine residues: Ser16, Ser25 and Ser38, located in the N-terminus region, and Ser63 at the beginning of the C-terminal domain of stathmin. To analyze the amounts of all phosphoforms of stathmin, we examined protein content of cells by Western-blot in denaturing conditions using antibodies against anti-stathmin phosphorylated on serine 16 (‘pSer16’), serine 25 (‘pSer25’), serine 38 (‘pSer38’) and serine 63 (‘pSer63’) (Fig. S2A). We observed that pSer38- and pSer25-stathmin were the main phosphoforms in our cell model. The higher phosphorylation levels of stathmin were weakly represented (for pSer16-stathmin) or undetectable (for pSer63-stathmin). Our results are consistent with expected ratios of phosphoforms of stathmin (11,13,14). We then performed indirect immunofluorescence of α-tubulin and pSer38-, pSer25- and pSer16-stathmin in fixed cells. Since no phosphorylation of Ser63 was observed by Western blot, pSer63-stathmin was not included in this assay. The quantification and distribution of NFRET hotspots between MTs and the cytosol are reported in Fig. 2. For FRET analysis, we selected two quantitative parameters: the number of NFRET hotspots belonging to MTs or the cytosol, and the percentage of MT plus-ends presenting NFRET hotspots. Images showing the NFRET distributions in cells were merged with the tubulin/MT-labeling images, and ROIs of 200 μm^2 were outlined in the cell periplasm. NFRET hotspots co-localizing with MTs and outside MTs (‘in the cytosol’) were counted and expressed per unit surface area (μm^2) of MT or cytosol (see ‘Materials and Methods for details). From the

same ROIs, a 0.5 µm long segment was drawn on the plus-end of MTs, and a NFRET hotspot was counted each time that one occurred in this calibrated area. For the immunofluorescence of total-stathmin, the density of NFRET hotspots in the cytosol was 1.0 ± 0.1 hotspots/µm^2 (Fig. 2A, white bars). The density of NFRET hotspots on MTs was significantly higher (1.5 ± 0.2 hotspots/µm^2, Fig. 2B) than in the cytosol. Our data indicate an appreciable fraction of stathmin interacting with the MT wall. Moreover, up to 82% of MT plus-ends showed NFRET hotspots (Fig. 2C), which is consistent with the presence of highly dynamic MTs in the cell periphery (38,39).

For pSer38- and pSer25-stathmin (gray and black bars, respectively in Fig. 2A-C), we counted 1.0 ± 0.1 and 0.7 ± 0.1 NFRET hotspots/µm^2 on MTs respectively, and 0.1 ± 0.1 hotspots/µm^2 in the cytosol for both phospho-stathmins. Also, 37% and 17% of MT plus-ends with NFRET hotspots were measured for pSer38- and pSer25-stathmin, respectively. In cells labeled for pSer38- (left panel) and pSer25-stathmin (middle panel), NFRET images show a punctuated distribution of NFRET signals mainly on MTs (Fig. 2D, white arrows). Thus, pSer25- and/or pSer38-stathmin could bound to the wall in addition to the plus-ends of MTs. By contrast, for anti-pSer16 stathmin, the number of NFRET hotspots was very low (Fig. 2A-B), and no hotspots were co-localized with the MT plus-ends (Fig. 2C). This is consistent with a loss of interaction between tubulin/MT and pSer16-stathmin (17), suggesting that phosphorylation of Ser16 abolished the ability of stathmin to bind to tubulin and/or MTs. By contrast, the phosphorylation of Ser25 and/or Ser38 did not affect the binding of stathmin to tubulin or MTs (wall and tips).

To address the question of how stathmin interacts with the MT wall, we over-expressed in living cells two forms of stathmin truncated in either the C-terminus (ΔCter-stathmin coupled to EGFP, as donor) or the N-terminus (ΔNter-stathmin also coupled to EGFP) of the protein. Tubulin tagged with mCherry was co-expressed as an acceptor. To avoid any effect of phosphorylation, the ΔCter-stathmin was mutated on Ser16, 25, 38 and 63, and the ΔNter-stathmin on Ser63 to alanine. All the NFRET quantifications were performed directly in living cells. When cells expressed ΔCter-stathmin, a similar density of NFRET hotspots was measured on MTs (2.2 ± 0.8 hotspots/µm^2) (Fig. 3A) and in the cytosol (1.9 ± 0.9 hotspots/µm^2) (Fig. 3C, right panel) where many NFRET hotspots were observed in the cytosol (arrows in ROI1) and along the MTs (arrows in ROI2). These results suggest that the ΔCter-stathmin protein interacts similarly with cytosolic tubulin and MTs. On the other hand, the expression of ΔNter-stathmin led to 2.5 ± 0.7 hotspots/µm^2 on MTs (Fig. 3B), and 0.5 ± 0.2 hotspots/µm^2 in the cytosol (Fig. 3B). These data suggest that the deletion of the N-terminus domain of stathmin facilitates its binding to the MT wall. In the T2S complex, the N-terminal region of stathmin is known to bind to the exposed surface of α-tubulin. The steric hindrance between dimers of tubulin in a protofilament does not permit correct positioning of the N-terminus domain, and so the ΔNter-stathmin has an ability to bind

preferentially to the surfaces and/or structures of tubulin exposed on the MT wall. Dynamic molecular interactions are fundamental to all cellular processes. In cells, analyses of these interactions are frequently carried out using fluorescence recovery after photobleaching (FRAP). The binding exchange of stathmin with tubulin/MT was next investigated by FRAP.

A binding-dominant model describes stathmin-tubulin/microtubule interactions.

In FRAP imaging, the rate of fluorescence recovery indicates how fast neighboring fluorescent molecules fill a bleached zone. This mobility of proteins depends on both diffusion and potential binding interactions. In our study, FRAP experiments were carried out on full stathmin (coupled to EGFP) expressed by living cells that also expressed mCherry-tubulin in order to locate the bleaching spots on MTs more clearly.

We first evaluated the contribution of diffusion in the FRAP curve. In cells over-expressing EGFP-stathmin, we used two photobleaching spot sizes (radius 2 µm and 4 µm) and compared fluorescence recovery curves (Fig. S3). We observed that the two curves were closely similar for the two spot sizes. Data were fitted using a single exponential equation. They gave comparable fractions of fluorescence at equilibrium (small ROI: $C_{eq} = 0.13 \pm 0.01$; large ROI: $C_{eq} = 0.15 \pm 0.02$), and similar rate constants (small ROI: $k = 0.57 \pm 0.07$ s^{-1}; large ROI: $k = 0.49 \pm 0.06$ s^{-1}). These data indicate that the diffusion of free stathmin is so fast relative to its binding to MTs that it can be ignored. The time curve of fluorescence recovery is dominated by the binding reaction of stathmin with tubulin and/or MTs and other protein partners (kinases and/or phosphatases).

We then used the binding-dominant model to determine how EGFP-stathmin interacts with MTs. FRAP experiments were carried out in the presence of MTs *vs.* in their nocodazole-induced absence (Fig. 4 and Table 1). We note that EGFP-stathmin can be phosphorylated by the enzyme machinery of cells. With MTs ('stathmin + microtubules' in Table 1), $k^*_{on} < k_{off}$ for the binding phase ($k^*_{on} = 0.07 \pm 0.02$ s^{-1} and $k_{off} = 0.36 \pm 0.06$ s^{-1}) together with $C_{eq} = 0.13 \pm 0.01$ (the fraction of stathmin bound at equilibrium) are evidence that stathmin binds to tubulin/MTs. With nocodazole ('stathmin – microtubules' in Table 1), $k^*_{on} = 0.14 \pm 0.03$ s^{-1} $<< k_{off} = 1.29 \pm 0.12$ s^{-1}, together with the decreased $C_{eq} = 0.10 \pm 0.01$, indicate a faster binding exchange of the stathmin/tubulin complexes and other protein partners than with MTs. The longer $t_{1/2}$ (1.91 ± 0.30 s) obtained with MTs than without them ($t_{1/2} = 0.54 \pm 0.05$ s) also shows that stathmin binds more strongly to tubulin when MTs are assembled.

When the MT polymerization is prevented by nocodazole, disappearance of the hyperphosphorylation forms and a progressive decrease in stathmin phosphorylation on Ser16 are observed (Küntziger et al., 2001). Here, the decrease in hyperphosphorylation forms of stathmin did not offset the lack of MT: the overall binding process of stathmin was reduced. Under regular conditions (no drug) a large proportion of stathmin forms are bound to MTs, and a smaller share to soluble tubulin dimers.

FRAP experiments with ΔCter-stathmin and ΔNter-stathmin with and without MTs were also conducted (Table 1). For ΔCter-stathmin with and without MTs, similar short $t_{1/2}$ (0.63 ± 0.05 s and 0.40 ± 0.02 s, respectively), $k^*_{on} << k_{off}$, and C_{eq} values (0.05 ± 0.01 and 0.04 ± 0.01, respectively) were measured. With or without MTs, FRAP parameters were similar, suggesting that the N-terminal domain of stathmin binds preferentially to the soluble tubulin dimers. In addition, FRAP analysis of ΔNter-stathmin in the presence of MTs gave a 2.6-fold lower k_{off} (0.61 ± 0.06 s^{-1}) and 2.6-fold longer $t_{1/2}$ (1.13 ± 0.11 s) than without MT (k_{off} = 1.59 ± 0.08 s^{-1} and $t_{1/2}$ = 0.44 ± 0.1 s). The value of C_{eq} = 0.14 ± 0.01 was significantly higher than that without MT (C_{eq} = 0.04 ± 0.01). These data are comparable to those obtained with EGFP-stathmin obtained in the presence of MTs, indicating an appreciable fraction of stathmin interacting with the MT wall.

FRAP analysis showed that exchange at the binding site of stathmin is significantly modified by the presence of MTs, and that the C-terminal domain of stathmin is involved in this reaction. The above experiments yield compelling evidence that stathmin can bind to MTs in cells. We then sought to elucidate how the MT dynamics and their structure were involved in this interaction. For this purpose we used taxol, a well-known ligand able to stabilize MTs and change dynamics.

The interaction of pSer25- and/or pSer38-stathmin with microtubules is promoted by a low concentration of taxol.

It is well established that the structure and stability of MTs are modified by the binding of taxol (40). Taxol also induces an increase in stathmin phosphorylation (41,42). To further explore the molecular mechanism of the binding of stathmin to MTs, cells were exposed to 1–50 nM taxol (4 h at 37 °C) to determine a concentration of taxol that disturbed the MT dynamics without modifying the phosphorylation of stathmin. Non-denaturing Western blots revealed that in cells incubated with 1 nM and 3.5 nM of taxol, the phosphorylation levels of stathmin did not change compared with untreated cells (Fig. S2B). Beyond 3.5 nM taxol, tri- and tetra-phosphorylated stathmin increased significantly, indicating large amounts of pSer16- and pSer63-stathmin. In addition, parameters of the MT dynamics were measured (Table S1). Compared with untreated cells, 1 nM taxol did not modify the rate of shrinkage or the time spent in shortening phases, whereas longer pause and shorter growing time (32%) were recorded. Higher concentrations of taxol caused lower rates of shrinkage (up to −52%, at 20 nM taxol).

For the immuno-FRET experiment, we analysed the ability of stathmin (using ‘total-stathmin’ labelling) and pSer25-/pSer38-stathmin (using specific phosphoform labelling) to interact with tubulin and MTs in the presence of 1nM taxol (4h, 37°C) (Fig. 5). With 1 nM taxol, we found a 1.6-fold higher density of hotspots on MTs (2.4 ± 0.4 NFRET hotspots/µm^2, Fig. 5B black bar) compared with untreated cells (1.5 ± 0.2 hotspots/µm^2,

Fig.5D, white bar), showing a large number of NFRET hotspots on MTs (lower panel). No significant change in the number of NFRET hospots in the cytosol (1.0 ± 0.1 hotspots/µm^2 *vs.* 0.8 ± 0.2 hotspots/µm^2 with taxol, Fig. 5A) was found. The percentages of NFRET hotspots at MT plus-ends were comparable between untreated and 1 nM taxol-treated cells (82% and 95%, respectively) (Fig. 5C). These observations indicate that 1 nM taxol increases the binding of stathmin to the MT wall. Furthermore, we detected more NFRET hotspots for pSer38-stathmin (1.9 ± 0.2 hotspots/µm^2) and pSer25-stathmin (1.7 ± 0.1 hotspots/µm^2) in taxol-treated than in untreated cells (1.0 ± 0.1 NFRET hotspots/µm^2 for pSer38-stathmin, and 0.7 ± 0.1 NFRET hotspots/µm^2 for pSer25-stathmin). No significant change in the counted NFRET hotspots was measured in the cytosol (0.10 ± 0.10 hotspots/µm^2 *vs.* 0.15 ± 0.10 hotspots/µm^2 with 1 nM taxol, for the two phosphorylated stathmins). Thus, with 1 nM of taxol, the forms of stathmin interacting with MTs were mainly pSer25-/pSer38-stathmin. In addition, for pSer38- and pSer25-stathmin, 37% and 25% of MT plus-ends showed NFRET hotspots respectively, which was similar to untreated cells. Altogether, 1 nM taxol drastically increased the number of interactions of phosphorylated stathmin with the tubulin protofilaments and the plus-ends of MTs.

Our data reveal that in the presence of 1 nM taxol, pSer25- and/or pSer38-stathmin interacted largely with the MT wall and at the plus-ends. The increase in the fraction of stathmin bound to MTs could be related to significant changes in surfaces and/or structures of tubulin exposed on the MT wall and/or to a decrease in the MT dynamic instability mediated by taxol. Thus, our results suggest strongly that low concentration of taxol potentiated the interaction of stathmin by its C-terminal domain with the MT wall.

DISCUSSION

The binding of stathmin to tubulin/MT has been extensively studied using a broad variety of *in vitro* methods (6,43–45). Stathmin binds to two tubulin heterodimers to form the "curved" T2S tubulin sequestering complex. To date, clear proof of stathmin binding to tubulin/MTs is lacking, especially in cells where interactions depend on the microenvironment. Here, in A549 cells, we demonstrate by immuno-FRET and FRAP imaging that the interaction of stathmin with tubulin can occur not only in the cytosol, but also along the length and at the plus-end of MTs. This pattern had not been observed in cells before.

In a step toward understanding stathmin-tubulin/MT interactions in cells, we focused on the impact of the phosphorylation of stathmin. Recent *in vitro* data obtained from purified proteins indicate that di-pSer25-/pSer38-stathmin binds to pre-assembled MTs, unlike mono-pSer16- or pSer63-stathmin cannot (16,17). Furthermore, the catastrophe-promoting activity of stathmin cannot be disrupted by phosphorylation of Ser25 and Ser38. In our study, no significant NFRET signal was observed in cells when we used energy transfer between Ser16-phosphorylated stathmin and tubulin/MTs, confirming that stathmin does not bind to MT when phosphorylated on Ser16. We also found a significant quantity of pSer25- and/or pSer38-stathmin interacting with the plus-end and the wall of MT. The MT plus-end can be considered as an intermediate zone where a few curved protofilaments (interacting with unphosphorylated stathmin) coexist with laterally unbound protofilaments (interacting with pSer25- and/or pSer38-stathmin) (46). Furthermore, surfaces and/or structures of tubulin exposed on the MT wall seem to be more favorable for the binding of stathmin by its C-terminus domain. This is strongly supported by the interaction of truncated ΔNter-stathmin, particularly abundant on MTs. In this study we also examined the effect of low concentration of taxol (1nM), an anticancer drug that modulates mechanical properties of MTs, also reported elsewhere (47,48), without changing the level of stathmin phosphorylation. Our FRET data mainly evidenced a strong increase in the interaction of pSer38- and/or pSer25-stathmin forms with MTs in the presence of this drug. Taxol could induce structural modifications of MTs with substantial effects on the accessibility and/or three-dimensional structure of the binding loci of pSer25- and/or pSer38-stathmin with the MT wall.

Despite the central role of stathmin in the regulation of the MT assembly-disassembly, no direct measurement of the binding exchange of stathmin with MTs in living cells has been yet reported. This is probably because of the difficulties met in detecting rapid stathmin-tubulin exchanges (49,50). Our systematic analysis of stathmin-tubulin/MT binding through a FRAP approach indicates that stathmin interaction with tubulin/MT in living cells is a very dynamic process, with a $t_{1/2}$ value of the order of 2 s. Also, FRAP analysis using truncated stathmin revealed similar $t_{1/2}$ values for the ΔNter-stathmin protein and full stathmin, but significantly shorter $t_{1/2}$ for the ΔCter-stathmin form with and without MTs. The ΔCter-stathmin should interact

very weakly with MTs ($k^*_{on} << k_{off}$). Our FRAP data provide compelling evidence that stathmin can bind by its C-terminal domain to MT.

From all thet findings reported here, we can propose a model for the mechanism by which stathmin and Ser25- and/or Sr38-phosphoisoforms interact with tubulin and/or MTs (Fig. 6, Assembly). Unphosphorylated stathmin binds to tubulin dimers, giving the "curved" T2S assembly-incompetent complex, which indirectly promotes "catastrophe" or MT disassembly. The phosphorylation of Ser16 and Ser63 by kinases (51) leads to an inactive stathmin (as revealed by the loss of the NFRET signal). Ser25 and Ser38 can first be phosphorylated by cyclin-dependent kinase in T2S (52), releasing the N-terminus domain of stathmin and diminishing a number of interactions with tubulin to induce changes in the three-dimensional structure of the curved T2S complex. This leads to a "straight" T2S complex that can be incorporated into MTs during the assembly step, as previously suggested (9). In addition, we cannot rule out the possibility that pSer25- and/or pSer38-stathmin bind directly to tubulin protofilaments by their C-termini (as revealed with NFRET hotspots with truncated stathmin). During the disassembly phase (Fig. 6, Disassembly), the pSer25- and/or pSer38-stathmin found next to the ruffled MT plus-end may be dephosphorylated by a protein kinase such as PP2A (53). This allows active non-phosphorylated stathmin forms to act at the tip of MT, favoring the formation of tightly curved protofilament (T2S complex) and contributing directly to the catastrophe event. Being already present on the protofilament of MT, stathmin will only need to be dephosphorylated in response to a signaling pathway to become fully active. The same molecular mechanism has been proposed for MCAK (mitotic centromere-associated kinesin, a depolymerizing protein), which rapidly targets MT plus-ends (54). Taken together, our observations made in cells are consistent with the earlier *in vitro* studies of Manna et al. showing binding of phosphorylated stathmin throughout the length of MT, and Gupta et al., who demonstrate an interaction of unphosphorylated stathmin with the MT plus-ends (6,17).

In conclusion, using FRET and FRAP measurements, we have found direct evidence for the interaction of stathmin with both the length and the plus-end of MTs in cells. Here we give a molecular basis for the understanding of the effects of stathmin on the MT cytoskeleton in eukaryotic cells. Our data show the co-existence of the two models of stathmin action, the tubulin-sequestering role and the catastrophe-promoting activities at the plus-ends of MT, and the existence of a new population of phospho-stathmin (pSer25- and/or pSer38-stathmin) capable of binding to MTs without depolymerizing them.

ACKNOWLEDGEMENTS

R.N. received fellowships from Région Provence Alpes Côtes d'Azur and from ONET Technologies. We thank Prof. André Sobel for the gift of the antisera containing rabbit polyclonal anti-pSer16, anti-pSer25 and anti-pSer38 antibodies. V.P. gratefully acknowledges the help of S. Boulay. We acknowledge the financial support of INCa, INSERM and DGOS (SIRIC label). The authors declare that they have no conflict of interest.

AUTHOR CONTRIBUTION

R.N., G.B. and S.B. carried out the experimental work; S.G. generated plasmids 'ΔCter-stathmin' and 'ΔNter-stathmin' in this study. R.N., G.B., S.B., P.B., F.D. and V.P. participated in the data analysis and interpretation; R.N., G.B., F.D. and V.P. participated in the concept and design of the research; R.N., G.B., P.B., F.D., H.K. and V.P. drafted the paper.

REFERENCES

1. Belmont, L. D. and Mitchison, T. J. (1996) Identification of a protein that interacts with tubulin dimers and increases the catastrophe rate of microtubules. *Cell* **84**, 623–631
2. Curmi, P. A., Andersen, S. S., Lachkar, S., Gavet, O., Karsenti, E., Knossow, M., and Sobel, A. (1997) The stathmin/tubulin interaction in vitro. *J. Biol. Chem.* **272**, 25029–25036
3. Devred, F., Tsvetkov, P. O., Barbier, P., Allegro, D., Horwitz, S. B., Makarov, A. A., and Peyrot, V. (2008) Stathmin/Op18 is a novel mediator of vinblastine activity. *FEBS Lett.* **582**, 2484–2488
4. Belletti, B. and Baldassarre, G. (2011) Stathmin: a protein with many tasks. New biomarker and potential target in cancer. *Expert Opin. Ther. Targets* **15**, 1249–1266
5. Gigant, B., Curmi, P. A., Martin-Barbey, C., Charbaut, E., Lachkar, S., Lebeau, L., Siavoshian, S., Sobel, A., and Knossow, M. (2000) The 4 A X-ray structure of a tubulin:stathmin-like domain complex. *Cell* **102**, 809–816
6. Gupta, K. K., Li, C., Duan, A., Alberico, E. O., Kim, O. V, Alber, M. S., and Goodson, H. V. (2013) Mechanism for the catastrophe-promoting activity of the microtubule destabilizer Op18/stathmin. *Proc. Natl. Acad. Sci. U. S. A.* **110**, 20449–20454
7. Howell, B., Larsson, N., Gullberg, M., and Cassimeris, L. (1999) Dissociation of the tubulin-sequestering and microtubule catastrophe-promoting activities of oncoprotein 18/stathmin. *Mol. Biol. Cell* **10**, 105–118
8. Cassimeris, L. (2002) The oncoprotein 18/stathmin family of microtubule destabilizers. *Curr. Opin. Cell Biol.* **14**, 18–24
9. Steinmetz, M. O., Kammerer, R. A., Jahnke, W., Goldie, K. N., Lustig, A., and van Oostrum, J. (2000) Op18/stathmin caps a kinked protofilament-like tubulin tetramer. *EMBO J.* **19**, 572–580
10. Sobel, A. (1991) Stathmin: a relay phosphoprotein for multiple signal transduction? *Trends Biochem. Sci.* **16**, 301–305
11. Marklund, U., Brattsand, G., Shingler, V., and Gullberg, M. (1993) Serine 25 of oncoprotein 18 is a major cytosolic target for the mitogen-activated protein kinase. *J. Biol. Chem.* **268**, 15039–15047
12. Larsson, N., Melander, H., Marklund, U., Osterman, O., and Gullberg, M. (1995) G2/M transition requires multisite phosphorylation of oncoprotein 18 by two distinct protein kinase systems. *J. Biol. Chem.* **270**, 14175–14183
13. Larsson, N., Marklund, U., Gradin, H. M., Brattsand, G., and Gullberg, M. (1997) Control of microtubule dynamics by oncoprotein 18: dissection of the regulatory role of multisite phosphorylation during mitosis. *Mol. Cell. Biol.* **17**, 5530–5539
14. Marklund, U., Larsson, N., Gradin, H. M., Brattsand, G., and Gullberg, M. (1996) Oncoprotein 18 is a

phosphorylation-responsive regulator of microtubule dynamics. *EMBO J.* **15**, 5290–5298

15. Honnappa, S., Jahnke, W., Seelig, J., and Steinmetz, M. O. (2006) Control of intrinsically disordered stathmin by multisite phosphorylation. *J. Biol. Chem.* **281**, 16078–16083
16. Manna, T., Thrower, D. A., Honnappa, S., Steinmetz, M. O., and Wilson, L. (2009) Regulation of microtubule dynamic instability in vitro by differentially phosphorylated stathmin. *J. Biol. Chem.* **284**, 15640–15649
17. Manna, T., Thrower, D., Miller, H. P., Curmi, P., and Wilson, L. (2006) Stathmin strongly increases the minus end catastrophe frequency and induces rapid treadmilling of bovine brain microtubules at steady state in vitro. *J. Biol. Chem.* **281**, 2071–2078
18. Stryer, L. and Haugland, R. P. (1967) Energy transfer: a spectroscopic ruler. *Proc. Natl. Acad. Sci. U. S. A.* **58**, 719–726
19. Niethammer, P., Bastiaens, P., and Karsenti, E. (2004) Stathmin-tubulin interaction gradients in motile and mitotic cells. *Science* **303**, 1862–1866
20. Kenworthy, A. K. (2001) Imaging protein-protein interactions using fluorescence resonance energy transfer microscopy. *Methods* **24**, 289–296
21. König, P., Krasteva, G., Tag, C., König, I. R., Arens, C., and Kummer, W. (2006) FRET-CLSM and double-labeling indirect immunofluorescence to detect close association of proteins in tissue sections. *Lab. Invest.* **86**, 853–864
22. Adebiyi, A., Zhao, G., Narayanan, D., Thomas-Gatewood, C. M., Bannister, J. P., and Jaggar, J. H. (2010) Isoform-selective physical coupling of TRPC3 channels to IP3 receptors in smooth muscle cells regulates arterial contractility. *Circ. Res.* **106**, 1603–1612
23. Leo, M. D., Bannister, J. P., Narayanan, D., Nair, A., Grubbs, J. E., Gabrick, K. S., Boop, F. A., and Jaggar, J. H. (2014) Dynamic regulation of β1 subunit trafficking controls vascular contractility. *Proc. Natl. Acad. Sci. U. S. A.* **111**, 2361–2366
24. Dompierre, J. P., Godin, J. D., Charrin, B. C., Cordelières, F. P., King, S. J., Humbert, S., and Saudou, F. (2007) Histone deacetylase 6 inhibition compensates for the transport deficit in Huntington's disease by increasing tubulin acetylation. *J. Neurosci. Off. J. Soc. Neurosci.* **27**, 3571–3583
25. Gavet, O., Ozon, S., Manceau, V., Lawler, S., Curmi, P., and Sobel, A. (1998) The stathmin phosphoprotein family: intracellular localization and effects on the microtubule network. *J. Cell Sci.* **111 (Pt 22)**, 3333–3346
26. Breuzard, G., Hubert, P., Nouar, R., De Bessa, T., Devred, F., Barbier, P., Sturgis, J. N., and Peyrot, V. (2013) Molecular mechanisms of Tau binding to microtubules and its role in microtubule dynamics in live cells. *J. Cell Sci.* **126**, 2810–281927. Otsu, N. (1979) A threshold selection method from gray-

level histograms. *IEEE Trans. Syst. Man. Cybern.* **9**, 62–66

28. Ostlund, R. E., Leung, J. T., and Hajek, S. V. (1979) Biochemical determination of tubulin-microtubule equilibrium in cultured cells. *Anal. Biochem.*

29. Youvan, D. C., Silva, C. M., Bilina, E., Coleman, W. J., Dilworth, M. R., and Yang, M. M. (1997) Calibration of fluorescence resonance energy transfer in microtcopy using genetically engineered GFP derivatives on nickel chelating beads. *Biotechnology* **3**, 1–18

30. Wouters, F. S., Verveer, P. J., and Bastiaens, P. I. (2001) Imaging biochemistry inside cells. *Trends Cell Biol.* **11**, 203–211

31. Feige, J. N., Sage, D., Wahli, W., Desvergne, B., and Gelman, L. (2005) PixFRET, an ImageJ plug-in for FRET calculation that can accommodate variations in spectral bleed-throughs. *Microsc. Res. Tech.* **68**, 51–58

32. Gordon, G. W., Berry, G., Liang, X. H., Levine, B., and Herman, B. (1998) Quantitative fluorescence resonance energy transfer measurements using fluorescence microscopy. *Biophys. J.* **74**, 2702–2713

33. Phair, R. D., Gorski, S. A., and Misteli, T. (2004) Measurement of dynamic protein binding to chromatin in vivo, using photobleaching microscopy. *Methods Enzymol.* **375**, 393–414

34. Sprague, B. L., Pego, R. L., Stavreva, D. A., and McNally, J. G. (2004) Analysis of binding reactions by fluorescence recovery after photobleaching. *Biophys. J.* **86**, 3473–3495

35. Hallen, M. A., Ho, J., Yankel, C. D., and Endow, S. A. (2008) Fluorescence recovery kinetic analysis of gamma-tubulin binding to the mitotic spindle. *Biophys. J.* **95**, 3048–3058

36. Wang, Y.-L. (2007) Noise-induced systematic errors in ratio imaging: serious artefacts and correction with multi-resolution denoising. *J. Microsc.* **228**, 123–131

37. Siegel, R. M., Chan, F. K., Zacharias, D. A., Swofford, R., Holmes, K. L., Tsien, R. Y., and Lenardo, M. J. (2000) Measurement of molecular interactions in living cells by fluorescence resonance energy transfer between variants of the green fluorescent protein. *Sci. STKE signal Transduct. Knowl. Environ.* **2000**, pl1

38. Sammak, P. J. and Borisy, G. G. (1988) Direct observation of microtubule dynamics in living cells. *Nature* **332**, 724–726

39. Walker, R. A., O'Brien, E. T., Pryer, N. K., Soboeiro, M. F., Voter, W. A., Erickson, H. P., and Salmon, E. D. (1988) Dynamic instability of individual microtubules analyzed by video light microscopy: rate constants and transition frequencies. *J. Cell Biol.* **107**, 1437–1448

40. Green, K. J. and Goldman, R. D. (1983) The effects of taxol on cytoskeletal components in cultured fibroblasts and epithelial cells. *Cell Motil.* **3**, 283–305

41. Küntziger, T., Gavet, O., Manceau, V., Sobel, A., and Bornens, M. (2001) Stathmin/Op18 phosphorylation is regulated by microtubule assembly. *Mol. Biol. Cell* **12**, 437–448

42. Martello, L. A., Verdier-Pinard, P., Shen, H.-J., He, L., Torres, K., Orr, G. A., and Horwitz, S. B. (2003) Elevated levels of microtubule destabilizing factors in a Taxol-resistant/dependent A549 cell line with an alpha-tubulin mutation. *Cancer Res.* **63**, 1207–1213
43. Wilson, L. and Correia, J. J. (2010) Microtubules, in vitro. Elsevier/Academic Press, Amsterdam; Boston
44. Barbier, P., Dorléans, A., Devred, F., Sanz, L., Allegro, D., Alfonso, C., Knossow, M., Peyrot, V., and Andreu, J. M. (2010) Stathmin and interfacial microtubule inhibitors recognize a naturally curved conformation of tubulin dimers. *J. Biol. Chem.* **285**, 31672–31681
45. Malesinski, S, Tsvetkov, P. O., Kruczynski, A., Peyrot, V., and Devred, F. (2015) Stathmin potentiates vinflunine and inhibits Paclitaxel activity. *PLoS One*. **10(6)**, e0128704
46. Mandelkow, E. M., Mandelkow, E., and Milligan, R. A. (1991) Microtubule dynamics and microtubule caps: a time-resolved cryo-electron microscopy study. *J. Cell Biol.* **114**, 977–991
47. Nogales, E., Wolf, S. G., Khan, I. A., Ludueña, R. F., and Downing, K. H. (1995) Structure of tubulin at 6.5 A and location of the taxol-binding site. *Nature* **375**, 424–427
48. Downing, K. H. and Nogales, E. (1998) New insights into microtubule structure and function from the atomic model of tubulin. *Eur. Biophys. J. EBJ* **27**, 431–436
49. Charbaut, E., Curmi, P. A., Ozon, S., Lachkar, S., Redeker, V., and Sobel, A. (2001) Stathmin family proteins display specific molecular and tubulin binding properties. *J. Biol. Chem.* **276**, 16146–16154
50. Krouglova, T., Amayed, P., Engelborghs, Y., and Carlier, M.-F. (2003) Fluorescence correlation spectroscopy analysis of the dynamics of tubulin interaction with RB3, a stathmin family protein. *FEBS Lett.* **546**, 365–368
51. Curmi, P. A., Gavet, O., Charbaut, E., Ozon, S., Lachkar-Colmerauer, S., Manceau, V., Siavoshian, S., Maucuer, A., and Sobel, A. (1999) Stathmin and its phosphoprotein family: general properties, biochemical and functional interaction with tubulin. *Cell Struct. Funct.* **24**, 345–357
52. Brattsand, G., Marklund, U., Nylander, K., Roos, G., and Gullberg, M. (1994) Cell-cycle-regulated phosphorylation of oncoprotein 18 on Ser16, Ser25 and Ser38. *Eur. J. Biochem.* **220**, 359–368
53. Mistry, S. J., Li, H. C., and Atweh, G. F. (1998) Role for protein phosphatases in the cell-cycle-regulated phosphorylation of stathmin. *Biochem. J.* **334 (Pt 1)**, 23–29
54. Helenius, J., Brouhard, G., Kalaidzidis, Y., Diez, S., and Howard, J. (2006) The depolymerizing kinesin MCAK uses lattice diffusion to rapidly target microtubule ends. *Nature* **441**, 115–119
55. Jourdain, L., Curmi, P., Sobel, A., Pantaloni, D., and Carlier, M. F. (1997) Stathmin: a tubulin-sequestering protein which forms a ternary T2S complex with two tubulin molecules. *Biochemistry* **36**, 10817–10821

CAPTION OF REGULAR FIGURES

Figure 1. FRET imaging detects stathmin-tubulin interactions in the cytosol, at the plus-end and along the length of MT walls. Immuno-FRET (A) and FRET by acceptor photobleaching (B) were performed following an indirect immunofluorescence of α-tubulin (FITC, as donor) and endogenous stathmin (TRITC, as acceptor), phosphorylated and unphosphorylated ('total-stathmin' on images). (A) The co-localization of α-tubulin (green) and endogenous stathmin (red) are juxtaposed to NFRET images (right); below, two regions of interest (ROI 1 and 2) with white arrows pointing to NFRET hotspots on MTs and in the cytosol and a blue arrowhead in ROI 1 to a NFRET hotspot at the MT plus-ends; for cropped NFRET images, the co-localization of NFRET hotspots with MTs and cytosolic tubulin are figured; side bars for NFRET intensities: color pixels (grey and purple) score for NFRET efficiencies from 0% to 5%. (B) The recovery of FITC (α-tubulin) emission after TRITC (total-stathmin) photobleaching confirms the NFRET signal in the initial state: the comparison of fluorescence intensities of FITC-labeled α-tubulin between pre- and post-bleaching of TRITC-labeled stathmin (white arrows) reveals a fluorescence recovery of donor in spots on MTs; no relevant fluorescence intensity fluctuation is observed inside the 'control' regions. Side bars: color pixels score for fluorescence intensity in 256 colored levels. Scale bar for (A-B): 15 µm.

Figure 2. Stathmin interacting with MTs is phosphorylated on serine 38 and/or 25. Immuno-FRET of α-tubulin and stathmin using primary antibodies specific for serine 38 (pSer38), 25 (pSer25) and 16 (pSer16) phosphoforms of stathmin was performed. Numbers of NFRET hotspots located in the cytosol (A) and on MT (B); each reported value corresponds to the mean number ± s.e.m of NFRET hotspots counted in 40 ROIs of 200 μm^2, a ROI per cells, and expressed per μm^2 of MT or cytosol. Bars refer to immunofluorescence of total-stathmin (white bars), pSer38-stathmin (gray bars), pSer25-stathmin (black bars), pSer16-stathmin (hatched bars). (C) Percentages of MT plus-ends displaying NFRET hotspots (means ± s.e.m of 100 MTs from 20 ROIs); significant statistical differences (*) were calculated using Student's t test with $p < 0.01$. (D) Images showing the superimposition of immunofluorescence of α-tubulin and phosphoforms of stathmin (upper panels), the distribution of NFRET hotspots (middle panels) and the superimposition of NFRET signal with the α-tubulin labelling (lower panels): the bound forms of pSer25- and/or pSer38-stathmin are mainly located on the MT wall (white arrows), whereas no NFRET hotspots for pSer16-stathmin are detected (white empty arrowheads) despite co-localization with tubulin/MTs; side bars for NFRET intensities: color pixels (grey and purple) score for NFRET efficiencies from 0% to 5%; scale bars: 5 µm.

Figure 3. Stathmin can interact by its C-terminal domain with the MT. (A-B) Living cells co-overexpressing truncated EGFP-ΔCter-stathmin (A), EGFP-ΔNter-stathmin (B) forms (as donor) and mCherry-tubulin (as acceptor); each reported value corresponds to the mean ± SD number of NFRET hotspots counted in 18 ROIs of 200 µm^2, a ROI per cells, and expressed per µm^2 of MT (white bars) or cytosol (black bars); the significant statistical difference (**) was calculated using Student's t test with $p < 0.001$. (C) Data are illustrated by a representative head image with two enlarged ROIs underneath (panels on the right): white arrows show NFRET hotspots on MTs. White arrowheads point to hotspots in cytosol; side bars for NFRET intensities: color pixels (gray and purple) score for NFRET efficiencies from 0% to 12%; scale bars: 10 µm.

Figure 4. FRAP curves reveal a binding-dominant model of stathmin with tubulin/MTs. After photobleaching, fluorescence intensity of EGFP-stathmin corresponding to the full stathmin was plotted against time. The fluorescence recovery of EGFP-stathmin was monitored in the presence (filled circle) or in the absence (empty circle) of the MT network. MTs were disassembled by nocodazole (1 mg/ml for 30 minutes and maintained in medium during FRAP experiments). The full line curves correspond to the average fit of 10–15 recovery courses. Compared with no MT, an apparent longer half-time $t_{1/2}$ of the stathmin fluorescence measured with MTs shows a slower binding exchange of the complex stathmin/MTs than stathmin/tubulin dimers in the cytosol.

Figure 5. The interaction of pSer38- and/or pSer25-stathmin with the MTs is promoted by taxol. Immuno-FRET of α-tubulin and stathmin (for total-stathmin, pSer38-stathmin and pSer25-stathmin) was performed on cells incubated without (white bars) and with 1 nM taxol (black bars) (4 h, 37 °C). Numbers of NFRET hotspots located in the cytosol (A) and on MT (B); each reported value corresponds to the mean ± s.e.m number of NFRET hotspots counted in 40 ROIs of 200 µm^2, a ROI per cells, and expressed per µm^2 of MT or cytosol. (C) Percentages of MT plus-ends displaying NFRET hotspots (means ± s.e.m of 100 MTs from 20 ROIs); significant statistical differences (*) were calculated using Student's t test with $p < 0.01$. (D) All data are illustrated with (D) panels of images on the right; side bars for NFRET intensities: color pixels (gray and purple) score for NFRET efficiencies from 0% to 5%; scale bars: 5 µm.

Figure 6. Conceptual model for the catastrophe-promoting mechanism by which stathmin depolymerizes MTs. Data in cells show that the interaction of stathmin with tubulin/MTs is modulated by its phosphorylation status (numbers in brackets refer to the figure above): [1] Binding of stathmin (green) to tubulin promotes MT catastrophe by sequestering free tubulin [1a] (NFRET hotspots) and by acting on protofilaments at MT plus-ends, thus destabilizing the tips and increasing the likelihood of catastrophe [1b] (6,55); [2a] Binding of pSer25-

/pSer38-stathmin (orange) to MT wall constitutes a pool of inactive stathmin (NFRET hotspots), possibly a scaffold with phosphatases (53), dephosphorylated and contributing to the catastrophe; or [2b] phosphorylation of Ser25 and/or Ser38 of stathmin by kinases may change curved to “straight” T2S complex so it can be incorporated into the growing MT (16,51); [3] fully phosphorylated stathmin detaches from tubulin/MTs and is unable either to sequester tubulin or to promote MT disassembly (51).

Table 1. Dynamic of interaction of stathmin with tubulin/MT: photobleaching analysis.

Conditions	**F_∞**	**C_{eq}**	**k_{off} (s^{-1})**	**k^*_{on} (s^{-1})**	**$t_{1/2}$ (s)**
stathmin + microtubules	0.91 ± 0.01	0.13 ± 0.01	0.36 ± 0.06	0.07 ± 0.02	1.91 ± 0.30
stathmin - microtubule	0.94 ± 0.01	0.10 ± 0.01	1.29 ± 0.12	0.14 ± 0.03	0.54 ± 0.05
ΔCter-stathmin + microtubules	0.90 ± 0.01	0.05 ± 0.01	1.09 ± 0.09	0.05 ± 0.02	0.63 ± 0.05
ΔCter-stathmin - microtubule	0.88 ± 0.01	0.04 ± 0.01	1.76 ± 0.09	0.07 ± 0.03	0.40 ± 0.02
ΔNter-stathmin + microtubules	0.94 ± 0.01	0.14 ± 0.01	0.61 ± 0.06	0.10 ± 0.02	1.13 ± 0.11
ΔNter-stathmin - microtubule	0.90 ± 0.01	0.04 ± 0.01	1.59 ± 0.08	0.07 ± 0.02	0.44 ± 0.03

The condition 'X - microtubule' corresponds to cells treated with 1 ng/µL nocodazole (30 min before and maintained during FRAP experiment) to disassemble microtubules. Background-subtracted fluorescence intensities of stathmin and its truncated forms after photobleaching as a function of time was fitted with a single exponential to obtain the fractions of fluorescence at equilibrium due to binding C_{eq}, the dissociation rate constant k_{off}, and the fluorescence intensity F_∞ (at time ~10 s, end of recording) in the presence or in the absence of microtubules. Values represent means ± standard error. The number of experiments for each datum point varied from 7 to 15 recovery curves (n = 7 – 15 cells). *ΔNter-stathmin*, stathmin deleted from Met1 to Ser40 plus from Glu141 to Asp149 and mutated on Ser63 to alanine; *ΔCter-stathmin*, stathmin deleted from Lys100 to Glu147 and mutated on Ser16, 25, 38, 63 to alanine.

Figure 1

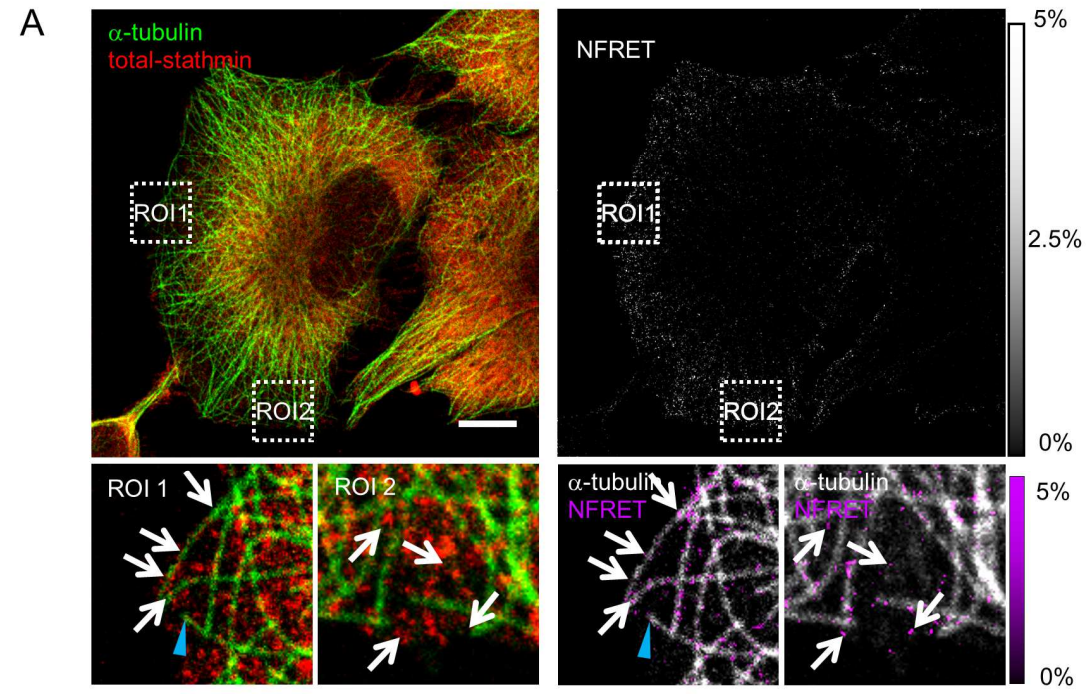
A
α-tubulin
total-stathmin
ROI1
ROI2
NFRET
5%
2.5%
0%
ROI 1
ROI 2
α-tubulin
NFRET
α-tubulin
NFRET
5%
0%

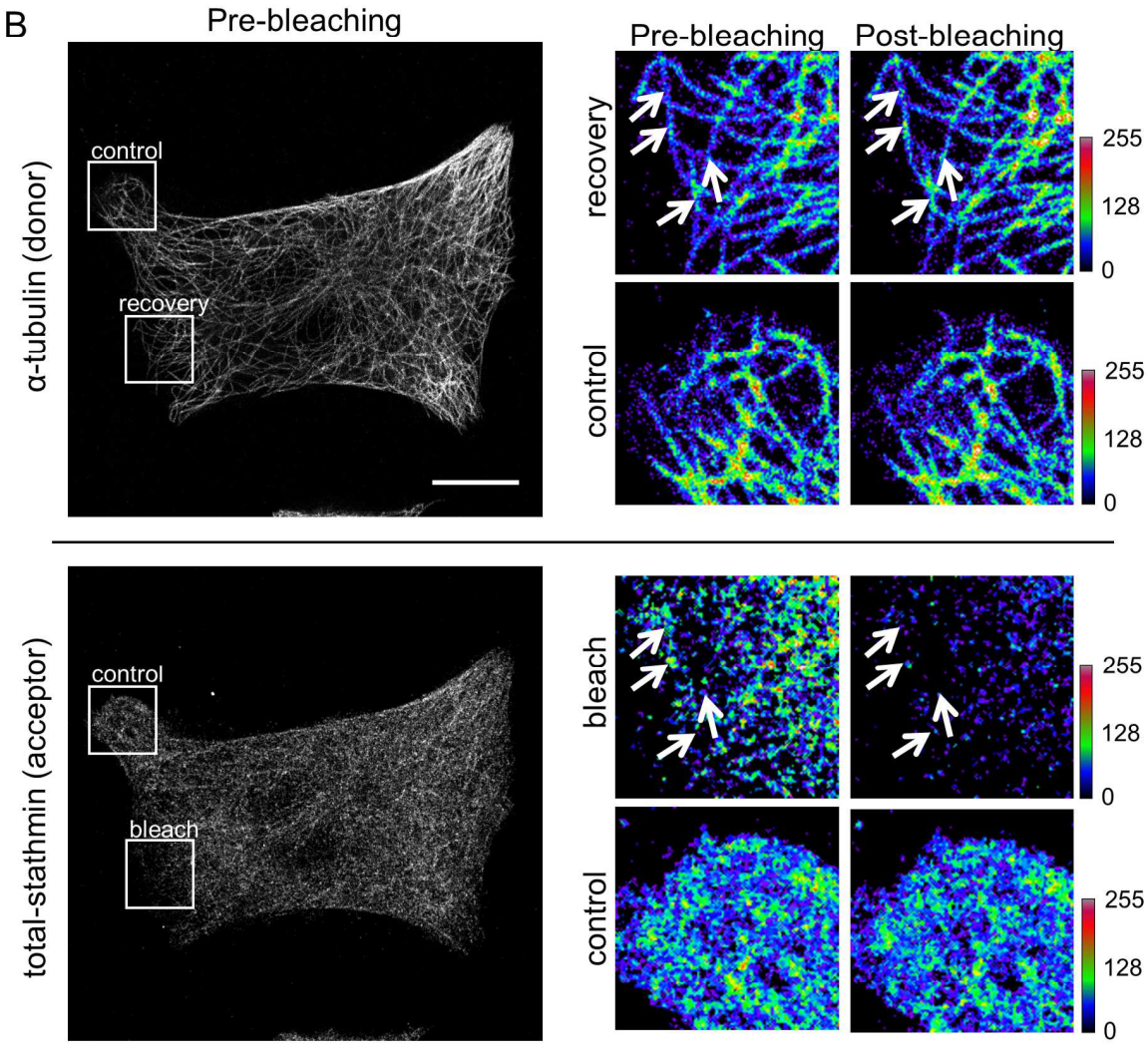
B
Pre-bleaching
α-tubulin (donor)
control
recovery
Pre-bleaching
Post-bleaching
recovery
control
255
128
0
255
128
0
total-stathmin (acceptor)
control
bleach
bleach
control
255
128
0
255
128
0

Figure 2

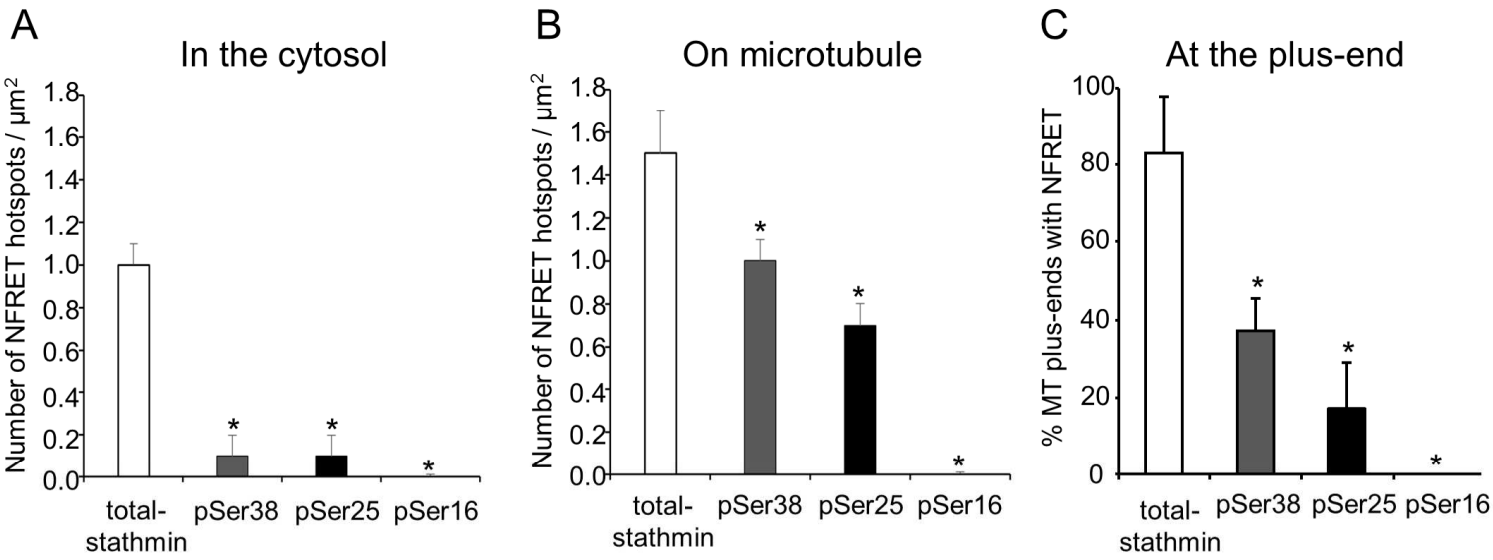
A
In the cytosol
Number of NFRET hotspots / µm²
1.8
1.6
1.4
1.2
1.0
0.8
0.6
0.4
0.2
0.0
*
*
*
total-stathmin
pSer38
pSer25
pSer16
B
On microtubule
Number of NFRET hotspots / µm²
1.8
1.6
1.4
1.2
1.0
0.8
0.6
0.4
0.2
0.0
*
*
*
total-stathmin
pSer38
pSer25
pSer16
C
At the plus-end
% MT plus-ends with NFRET
100
80
60
40
20
0
*
*
*
total-stathmin
pSer38
pSer25
pSer16

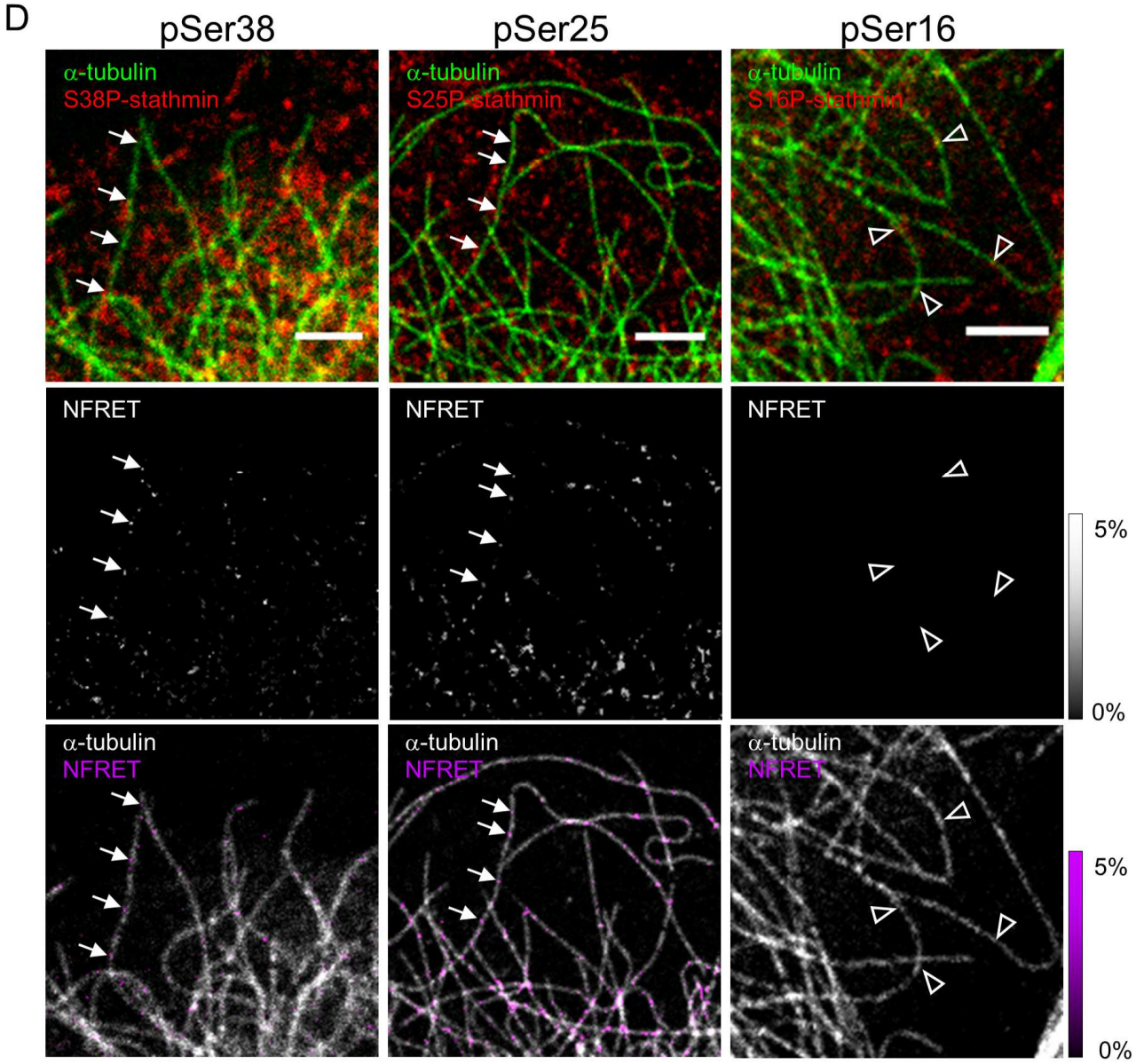
D
pSer38
pSer25
pSer16
α-tubulin
S38P-stathmin
α-tubulin
S25P-stathmin
α-tubulin
S16P-stathmin
NFRET
NFRET
NFRET
5%
0%
α-tubulin
NFRET
α-tubulin
NFRET
α-tubulin
NFRET
5%
0%

Figure 3

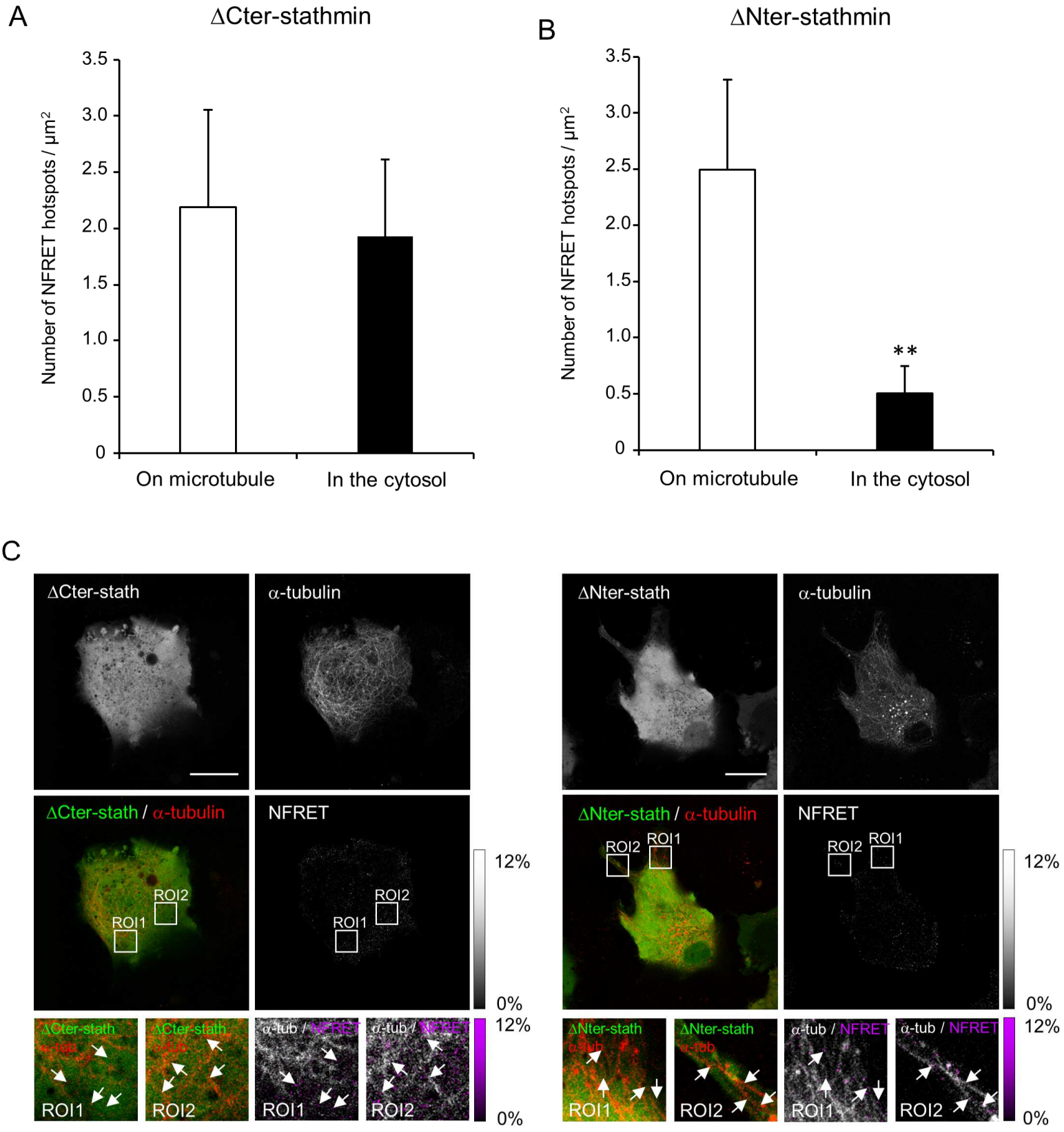
A
ΔCter-stathmin
Number of NFRET hotspots / µm²
3.5
3.0
2.5
2.0
1.5
1.0
0.5
0
On microtubule
In the cytosol
B
ΔNter-stathmin
Number of NFRET hotspots / µm²
**
On microtubule
In the cytosol
C
ΔCter-stath
α-tubulin
ΔCter-stath / α-tubulin
NFRET
ROI1
ROI2
12%
0%
ΔNter-stath
α-tubulin
ΔNter-stath / α-tubulin
NFRET
ROI1
ROI2
12%
0%

Figure 4

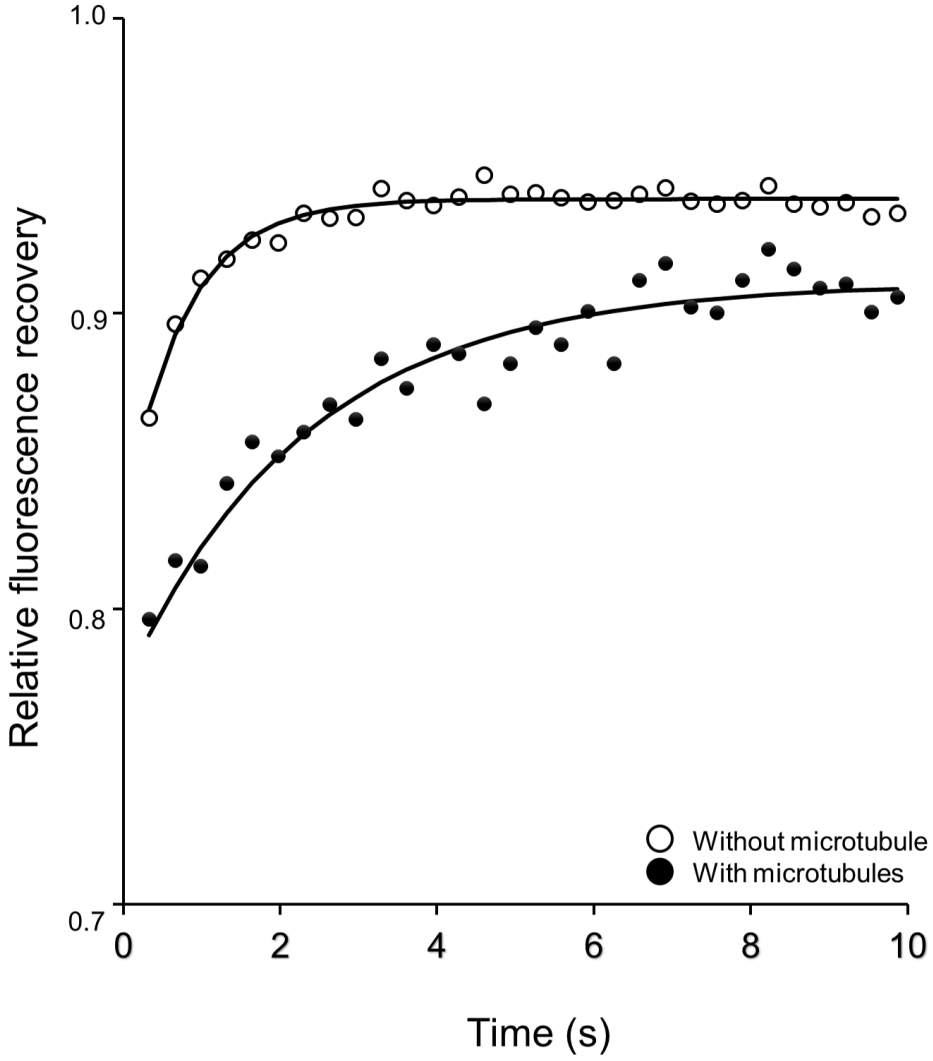
1.0
0.9
0.8
0.7
Relative fluorescence recovery
0
2
4
6
8
10
Time (s)
Without microtubule
With microtubules

Figure 5

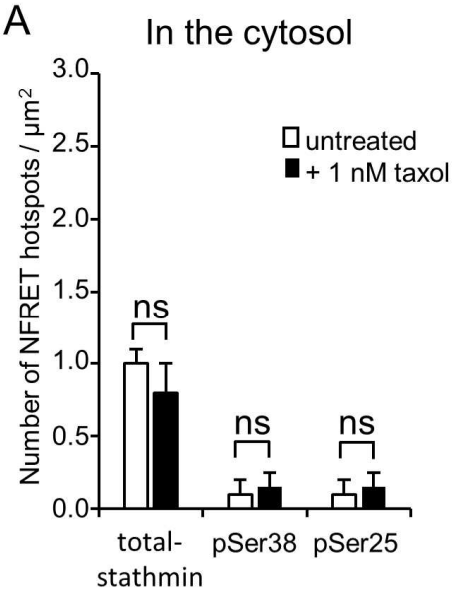
A
In the cytosol
Number of NFRET hotspots / µm²
3.0
2.5
2.0
1.5
1.0
0.5
0.0
untreated
+ 1 nM taxol
ns
ns
ns
total-stathmin
pSer38
pSer25

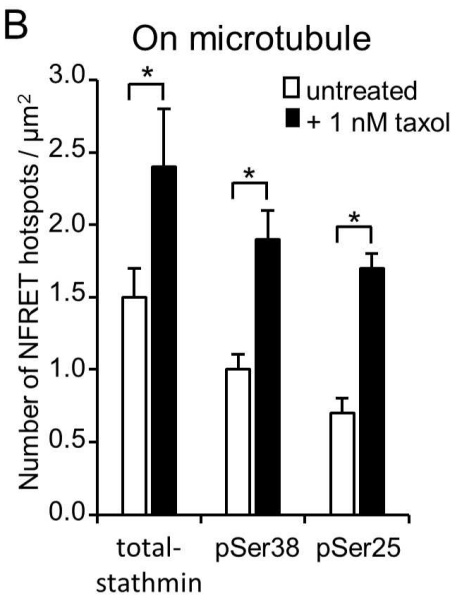
B
On microtubule
Number of NFRET hotspots / µm²
3.0
2.5
2.0
1.5
1.0
0.5
0.0
untreated
+ 1 nM taxol
*
*
*
total-stathmin
pSer38
pSer25

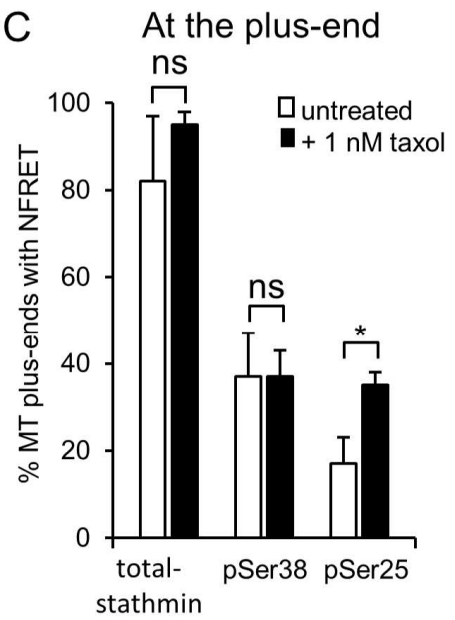
C
At the plus-end
% MT plus-ends with NFRET
100
80
60
40
20
0
untreated
+ 1 nM taxol
ns
ns
*
total-stathmin
pSer38
pSer25

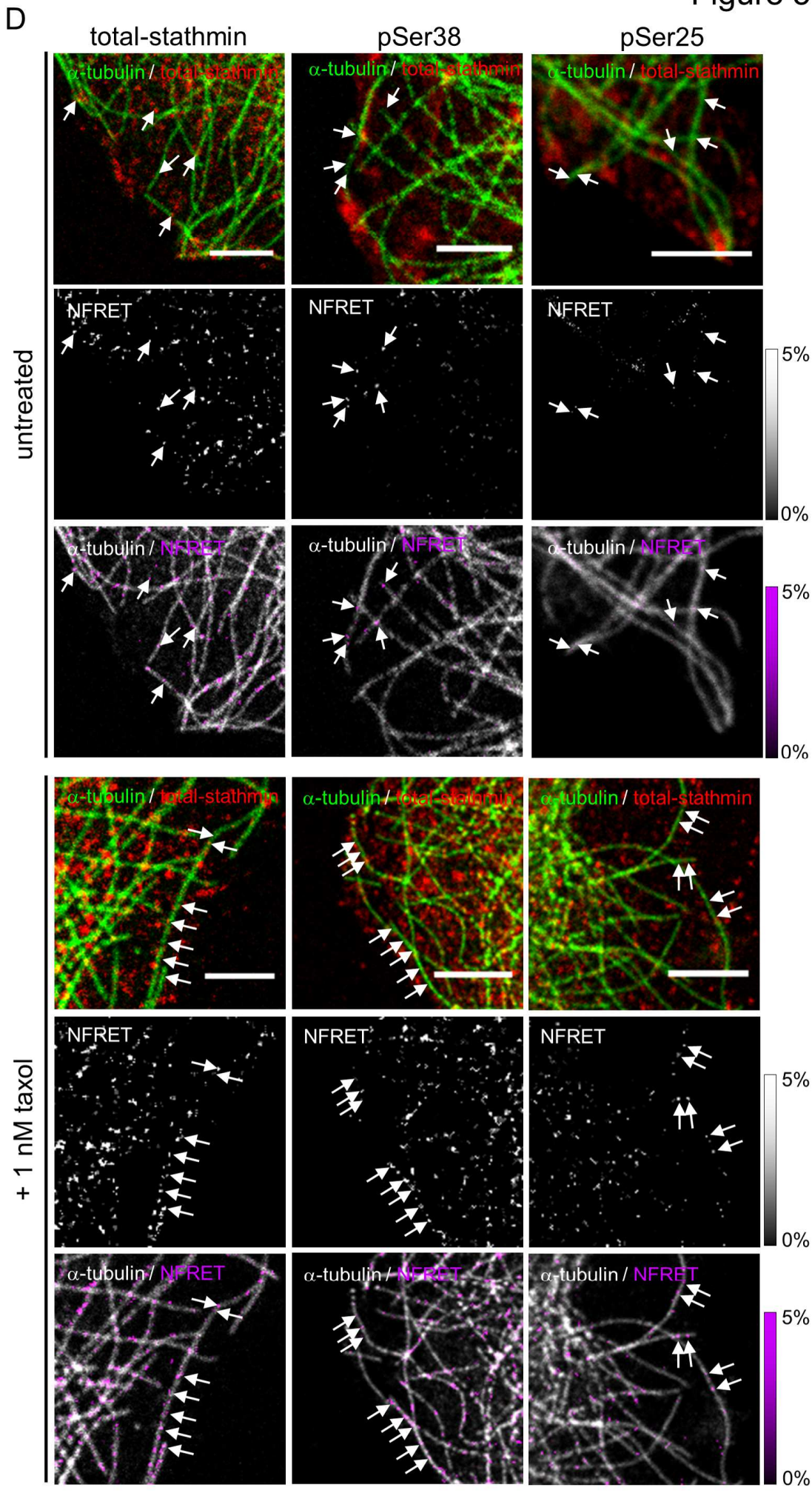
D
total-stathmin
pSer38
pSer25
untreated
+ 1 nM taxol
α-tubulin / total-stathmin
NFRET
α-tubulin / NFRET
5%
0%

Figure 6

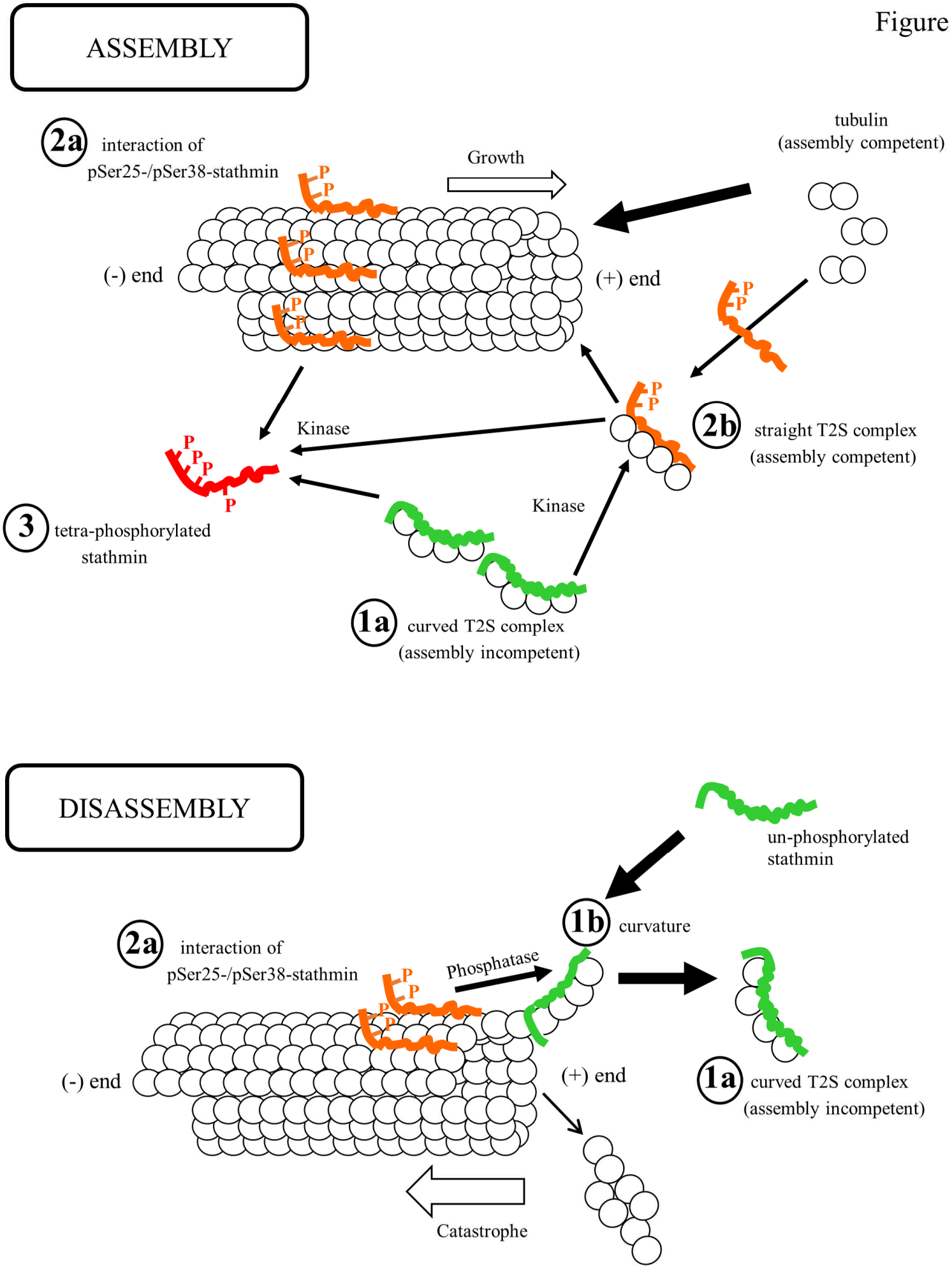
ASSEMBLY
2a interaction of pSer25-/pSer38-stathmin
Growth
tubulin (assembly competent)
(-) end
(+) end
P
Kinase
2b straight T2S complex (assembly competent)
3 tetra-phosphorylated stathmin
Kinase
1a curved T2S complex (assembly incompetent)
DISASSEMBLY
un-phosphorylated stathmin
1b curvature
2a interaction of pSer25-/pSer38-stathmin
Phosphatase
(-) end
(+) end
1a curved T2S complex (assembly incompetent)
Catastrophe

Supplemental figure S1

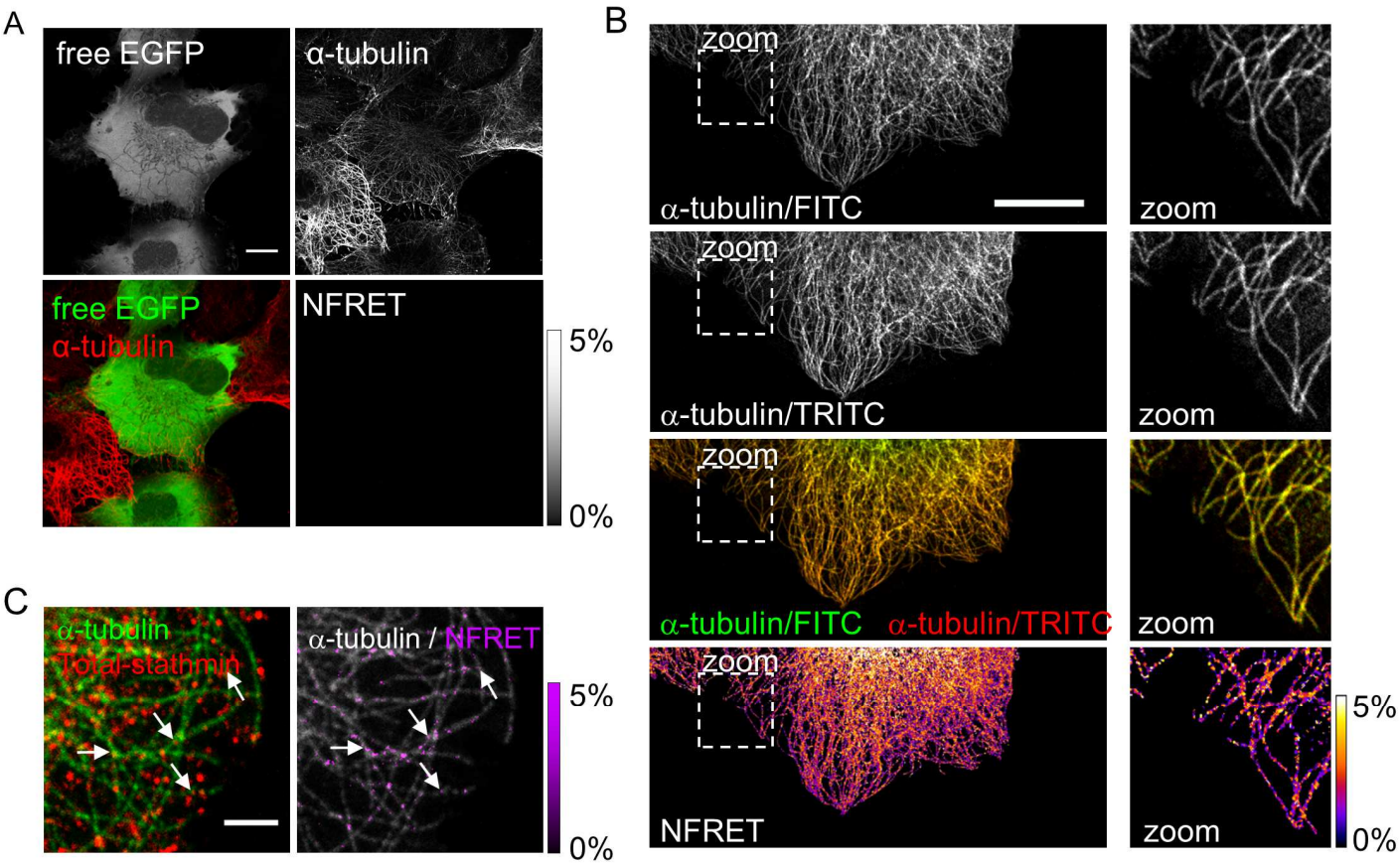

Figure S1. Three assays confirming the existence of NFRET hotspots. (A) No energy transfer between free EGFP and immuno-labeled α-tubulin despite their apparent co-localization: cells expressing free EGFP (as donor) were fixed and followed by an indirect immunofluorescence of α-tubulin (with a secondary antibody coupled to TRITC, as acceptor): no interaction is observed between EGFP and fluorescent MTs; side bars for NFRET intensities: pixels scoring for NFRET efficiencies from 0% (black) to 5% (white). (B) A quite homogeneous NFRET efficiency for two-colored α-tubulin: indirect immunofluorescence of α-tubulin was performed using two sets of secondary antibodies coupled to FITC (as donor) and TRITC (as acceptor); side bars for NFRET intensities: color pixels scoring for NFRET efficiencies from 0% (dark blue) to 5% (white). The NFRET intensity was spread over the MTs, with a range of NFRET efficiency between 1% and 5%. (C) A direct immunofluorescence of α-tubulin and total-stathmin still shows NFRET hotspots on MTs and in the cytosol: α-tubulin and total-stathmin were directly immuno-labeled with primary antibodies coupled to FITC (as donor) and Atto532 (as acceptor). Direct and indirect immunofluorescence of proteins show a similar distribution of NFRET hotspots on MTs and in the cytosol (white arrows) as for indirect immunofluorescence of proteins. This indicates that NFRET efficiency did not involve size and misorientation of the secondary antibody-antibody complexes in the indirect immunofluorescence; side bars for NFRET intensities: purple pixels score for NFRET efficiencies from 0% to 5%. For (A and B): scale bar referred to 15 µm, for (C), scale bar: 5 µm.

Supplemental figure S2

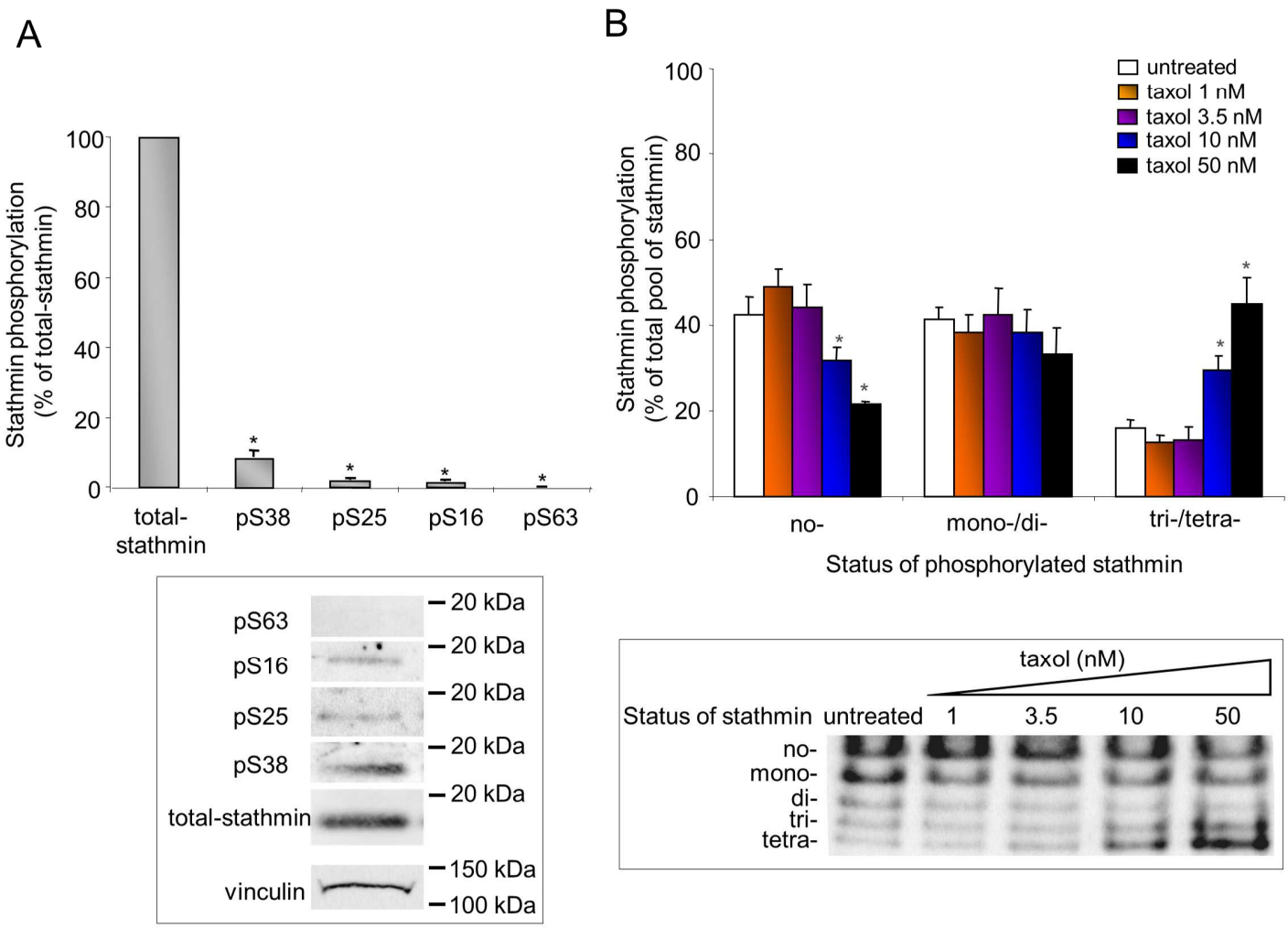

Figure S2. Ratios of phosphoforms of stathmin in A549 cells. (A) Cells were lyzed and protein contents were analyzed by Western-blot in denaturing conditions using antibodies against anti-total-stathmin ('total-stathmin') and anti-stathmin phosphorylated on serine 16 ('pS16'), serine 25 ('pS25'), serine 38 ('pS38'), and serine 63 ('pS63'); upper panel shows the amount of all phosphoforms of stathmin normalized to immunostained total-stathmin; lower panel displays a typical Western-blot experiment. (B) Cells were treated with 1 – 50 nM taxol for 4 h at 37°C, and then lyzed and protein contents were analyzed by Western-blot in non-denaturing conditions using anti-total-stathmin antibody; upper panel shows the amount of all phosphoforms of stathmin normalized to the total pool of stained stathmin; lower panel displays a typical Western-blot experiment; the labels 'no-', 'mono-', 'di-', 'tri-' and 'tetra-' denote states of un-, mono-, di-, tri- and tetra-phosphorylated stathmin, respectively. All significant statistical differences (*) were calculated using Student's *t* test with $p < 0.01$. Reported values correspond to mean ± SD of three independent experiments.

Supplemental figure S3

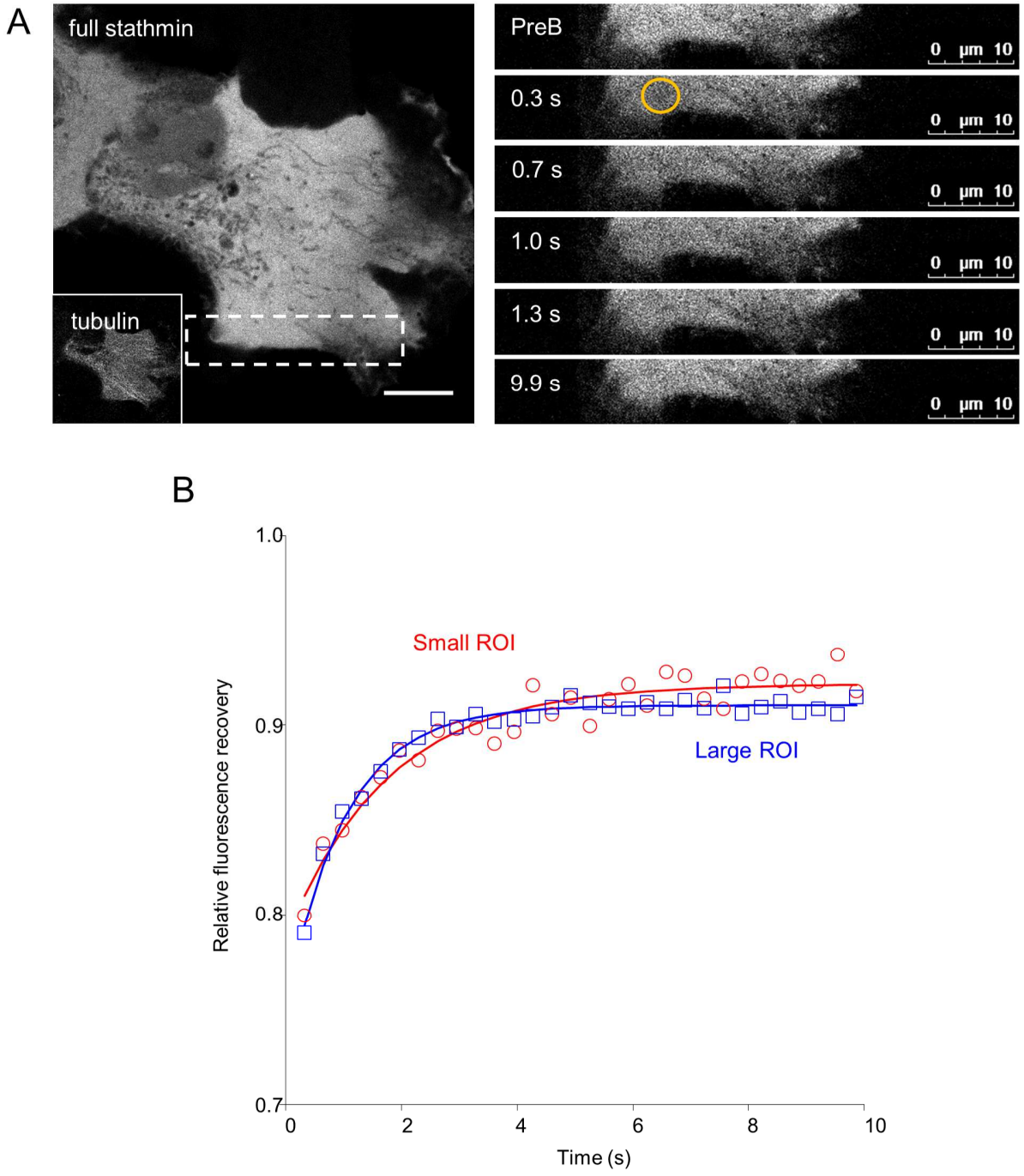

Figure S3. FRAP analysis of stathmin in the presence of MT. (A) left: enlarged view of stathmin fluorescence and MTs (inset); right: stathmin fluorescence recovery at exponentially increasing time points on the region containing MTs (ROI: 4 µm radius). (B) Mean data for small (2 µm radius) and large (4 µm radius) bleached ROIs, normalized to the first prebleach value, showing fluorescence recovery of stathmin. Recovery curves were fitted using a single exponential equation ($F(t) = F_{\infty} - C_{eq}.\exp^{-k.t}$) with no foreknowledge of either the geometry of the bleaching or the process of fluorescence recovery. Fits of data (small ROI, in red; large ROI, in blue) to the binding-dominant model give comparable fractions of fluorescence at equilibrium due to binding (small ROI: $C_{eq} = 0.13 \pm 0.01$; large ROI: $C_{eq} = 0.15 \pm 0.02$), dissociation rate constants (small ROI: $k = 0.57 \pm 0.07$ s^{-1}; large ROI: $k = 0.49 \pm 0.06$ s^{-1}), and fluorescence intensities (small ROI: $F\infty = 0.92 \pm 0.01$; large ROI: $F\infty = 0.91 \pm 0.01$). These features indicate that diffusion is not significantly limiting during recovery of stathmin in the presence of MT; recovery is instead dominated by binding interactions.

Table S1. Parameters of the MT dynamic instability in living cells.

Variables	Untreated	PTX 1 nM	PTX 3.5 nM	PTX 20 nM
Mean rates (µm/min)				
Growing	9.1 ± 0.4	8.4 ± 0.6	8.1 ± 0.7	6.3 ± 0.3 (-31%)
Shortening	11.7 ± 0.9	11.0 ± 1.0	8.5 ± 0.7 (-27%)	5.6 ± 0.3 (-52%)
% Time spent in				
Growing	37 ± 4	25 ± 3 (-32%)	21 ± 5 (-43%)	23 ± 3 (-38%)
Shortening	26 ± 4	26 ± 3	27 ± 4	30 ± 3
Pause	37 ± 3	49 ± 3 (+32%)	52 ± 5 (+40%)	47 ± 3 (+27%)
Overall dynamicity (µm/min)	4.6 ± 0.4	3.8 ± 0.4 (-18%)	3.0 ± 0.4 (-35%)	1.7 ± 0.1 (-63%)

Parameters of microtubule dynamic instability were measured at the cell periphery of living cells. The 'Untreated' refers to dynamicity parameters from cells expressing labelled tubulin, exclusively. Values are mean ± s.e.m of 50 microtubules. The results of three analogous experiments are presented. Numbers in brackets represent variations between cells expressing labelled α-tubulin ('Untreated') and other conditions, according to Student's t-test ($P = 0.05$).